**Title**

A Finite Element approach for determining the full load-displacement relationship of axially-loaded shallow screw anchors, incorporating installation effects

**Author list**

Benjamin Cerfontaine*, Jonathan A. Knappett, Michael J. Brown, Craig S. Davidson, Therar Al-Baghdadi, Yaseen U. Sharif, Andrew Brennan, Charles Augarde, William M. Coombs, Lei Wang, Anthony Blake, David J. Richards and Jon Ball

**Corresponding author*

**Author details**

Benjamin Cerfontaine, BSc, MSc, PhD

MSCA Research Fellow, School of Science and Engineering, University of Dundee, Fulton Building, Dundee, DD1 4HN, UK

ORCID: 0000-0002-4833-9412

Email: b.cerfontaine@dundee.ac.uk

Jonathan A. Knappett, MA MEng PhD GMICE

Professor, School of Science and Engineering, University of Dundee, Fulton Building, Dundee, DD1 4HN, UK

ORCID: 0000-0003-1936-881X

Email: j.a.knappett@dundee.ac.uk

Michael J. Brown, BEng PhD GMICE

Reader, School of Science and Engineering, University of Dundee, Fulton Building, Dundee, DD1 4HN, UK

ORCID: 0000-0001-6770-4836

Email: m.j.z.brown@dundee.ac.uk

Craig Davidson, BSc MSc

Research Associate, School of Science and Engineering, University of Dundee, Fulton Building, Dundee, DD1 4HN, UK

ORCID: 0000-0002-4843-5498

Email: c.s.davidson@dundee.ac.uk

Therar Al-Baghdadi, BSc, MSc, PhD

Geotechnical Engineer, Municipality of Karbala, Karbala, Iraq

ORCID: 0000-0002-7368-4285

Email: therarb@yahoo.co.uk

Yaseen U Sharif, BSc, MSc

PhD student, School of Science and Engineering, University of Dundee, Fulton Building, Dundee, DD1 4HN, UK

ORCID: 0000-0002-3620-7500

Email: y.u.sharif@dundee.ac.uk

Andrew J. Brennan, MEng PhD GMICE

Senior Lecturer, School of Science and Engineering, University of Dundee, Fulton Building, Dundee, DD1 4HN, UK

ORCID: 0000-0002-8322-0126

Email: a.j.brennan@dundee.ac.uk

Charles Augarde, BSc MSc DPhil CEng FICE

Professor, Department of Engineering, Durham University, Durham, DH1 3LE, UK

ORCID: 0000-0002-5576-7853

Email: charles.augarde@durham.ac.uk

Will M. Coombs, MEng PhD

Associate Professor, Department of Engineering, Durham University, Durham, DH1 3LE, UK

ORCID: 0000-0003-2099-1676

Email: w.m.coombs@durham.ac.uk

Lei Wang, PhD

Research Assistant, Department of Engineering, Durham University, Durham, DH1 3LE, UK

Email: lei.wang@durham.ac.uk

Anthony Blake, BEng, PhD

Research Fellow, Faculty of Engineering and the Environment, University of Southampton, SO17 1BJ, UK

ORCID: 0000-0001-5718-7900

Email: a.p.blake@soton.ac.uk

David J. Richards, BEng MSc PhD CEng MICE

Professor, Faculty of Engineering and the Environment, University of Southampton, UK

ORCID: 0000-0002-3819-7297

Email: djr@soton.ac.uk

Jon Ball, EurGeol Bsc. (Hons) CGeol FGS

Chief Geotehcnical Engineer, Roger Bullivant Ltd, Swadlincote, UK

Email: Jon.Ball@roger-bullivant.co.uk

**Main text word count:** 7602

**Number of tables:** 6

**Number of Figures:** 16



# A Finite Element approach for determining the full load-displacement relationship of axially-loaded shallow screw anchors, incorporating installation effects

B. Cerfontaine*, Jonathan A. Knappett, Michael J. Brown, Craig S. Davidson, Therar Al-Baghdadi, Andrew J. Brennan, Charles Augarde, William M. Coombs, Lei Wang, Anthony Blake, David J. Richards and Jon Ball

## ABSTRACT

Screw anchors have been recognised as an innovative solution to support offshore jacket structures and floating systems, due to their low noise installation and potential enhanced uplift capacity. Results published in the literature have shown that for both fixed and floating applications, the tension capacity is critical for design but may be poorly predicted by current empirical design approaches. These methods also do not capture the load-displacement behaviour, which is critical for quantifying performance under working loads. In this paper, a Finite Element methodology has been developed to predict the full tensile load-displacement response of shallow screw anchors installed in sand for practical use, incorporating the effects of a pitch-matched installation. The methodology is based on a two-step process. An initial simulation, based on wished-in-place conditions, enables the identification of the failure mechanism as well as the shear strain distribution at failure. A second simulation refines the anchor capacity using soil-soil interface finite elements along the failure surface previously identified and also models installation through successive loading/unloading of the screw anchor at different embedment depths. The methodology is validated against previously published centrifuge test results. A simplified numerical approach has been derived to approximate the results in a single step.

## KEYWORDS

Screw anchor, Helical Pile, Sand, Finite element modelling, Design

## INTRODUCTION

Screw anchors or piles are a foundation technology that may provide significant uplift capacity for offshore applications (Byrne and Houlsby 2015; Houlsby 2016) while avoiding pile driving nuisance for marine inhabitants (Bailey et al. 2010). Screw anchors consist of one or more steel helices (150-400mm diameter), attached to a core of smaller diameter and are used onshore to anchor relatively light structures (Perko 2009). These anchors are screwed into the soil by applying a torque and a crowd force to ensure penetration with a minimum soil disturbance (Perko 2009). Such anchors, if appropriately scaled-up, may be suitable to provide the very large tension requirements of bottom-fixed jacket structures (e.g. 20MN, (Byrne and Houlsby 2015)) or floating tension-leg platforms (e.g. 10MN, (Bachynski and Moan 2014)) for offshore wind turbines.

The uplift capacity of shallow screw anchors was investigated by Davidson et al. (2019) through centrifuge testing in medium-dense and dense sand. The centrifuge uplift capacities were compared with results published in the literature, as shown in Figure 1. This figure presents a non-dimensional bearing factor, $N_\gamma$, obtained by normalising the uplift capacity with respect to the helix embedment depth H, the area of the helix and the buoyant unit weight $\gamma'$,

$$N_\gamma = \frac{F_y}{\gamma' HA}. \tag{1}$$

Centrifuge results are consistent with the other experimental results, as shown in Figure 1. Bearing factors obtained by Ilamparuthi et al. (2002) constitute the upper bound of the results presented, especially at larger relative embedment. This is probably due to their relatively small scale, being tested at 1g, leading to a more pronounced effect of dilatancy on the soil response. Conversely, centrifuge tests provide a lower bound. Centrifuge results of Dickin (1988) were reported for comparison, but were related to square plate anchors, which have been shown to provide lower uplift capacity (Giampa et al. 2018a).

Byrne and Houlsby (2015) stated that multi-footing structures such as tripods or jacket structures will become necessary to deploy wind turbines in deeper water. In this case, the tensile capacity is the critical design case and screw anchors can provide sufficient capacity. However typical analytical approaches (e.g. Mitsch and Clemence 1985) may significantly overpredict the screw anchor capacity for these large scale applications. The recent semi-analytical method proposed by Giampa span style="font-family:Calibri; font-style:italic">et al. (2017) for shallow anchors which is based on peak friction and dilatancy angles for shallow anchors, assumes that the failure mechanism can be described by a shallow wedge, whose inclination to the vertical direction is equal to the dilatancy angle. This finding is similar to the work of White et al. (2008) for the uplift of buried pipelines and has been theoretically justified for anchors by Vermeer and Sutjiadi (1985). However, the method is limited to single helix screw anchors and does not provide any load-displacement (stiffness) information, which is very important for jacket structures and tension-leg platforms, as the axial stiffness controls the global rotational stiffness of the wind turbines. For instance, the rotation of bottom-fixed wind turbines must typically be kept below 0.5° to ensure safe operation (Achmus *et al.* 2009).

Finite Element modelling enables the prediction of the entire tensile load-displacement relationship, but few studies have previously tackled this problem for screw anchors in cohesionless soils due to the difficulties in capturing the effects of installation (a large displacement process) on capacity. Those approaches which have been proposed for modelling the problem rely on back-calculated parameters, characterising the soil properties around the anchor, to reproduce field or experimental tests (e.g. Papadopoulou et al. 2014; Mosquera et al. 2015; Perez et al. 2018) without which uplift capacities are overestimated (e.g. Gavin et al. 2014) due to an incorrect modelling of the strength mobilised at failure. On the other hand, the installation process is a large deformation process which strongly modifies the void ratio (e.g. tomography results presented in Schiavon (2016)) and stress state around the anchor, modifying the stiffness of the anchor. Giampa et al. (2017) used limit analysis and finite element methods to simulate small-scale 1g tests. However, they focused on anchor capacity and did not provide any comparison of the load-displacement behaviour/span> or initial stiffness. Consequently, there is a need to develop a new methodology to better predict both the uplift capacity and initial stiffness that does not rely physical testing for deriving global empirical parameters and which is simple enough to be used in the practical design of screw anchors.

The objective of this study is to define a flexible methodology to predict drained tensile performance of shallow screw anchors representative of offshore applications (full load-displacement behaviour, incorporating capacity and stiffness) using the Finite Element method in 2D axisymmetric conditions, which accounts for the effects of a drained installation process in a simplified way. This method is based on a well-defined numerical procedure requiring measurable, rather than arbitrarily defined soil parameters and is applicable to a range of geometries (helix number and spacing). This will address the key limitations of existing analytical and numerical capacity models and will provide a method for determining both stiffness (as necessary to calculate natural frequencies of a foundation-renewable device system) and capacity (i.e. a virtual load test) for informing practical design. Single and double large helix diameter screw anchor centrifuge load tests, published by (Davidson et al. 2020) and wished-in-place typical onshore screw anchors Hao et al. (2018), will be used to validate the finite element analyses. The shape of the failure mechanism, the stress and strain distributions along the failure mechanism are key variables that are studied in detail in order to develop a reliable method for design.

## PHYSICAL AND NUMERICAL MODELS

The Finite Element (FE) method cannot be used to reproduce the exact large-deformation installation process, with other methods being preferable (Wang et al. 2017). However, the FE method offers a good compromise between the simulation cost and accuracy of results. The objective of this work is to develop a modelling approach that is practically applicable in the design screw anchors for offshore applications. Consequently, it must be achievable within commercial software (e.g. PLAXIS software (PLAXIS 2017a)), it must be fast (2D axisymmetric analysis) and it must be based on typical constitutive models (e.g. the Hardening soil model (Schanz et al. 1999a)) relying on a limited number of measurable parameters that can be determined using routine laboratory ad in-situ test methods. The numerical modelling methodology as well as physical (centrifuge) models used to validate it are described in this section.

### *Centrifuge tests*

Numerical results are validated against two sets of small-scale centrifuge tests undertaken at the University of Dundee (UoD) (Davidson et al. 2019) and the University of Western Australia (UWA) (Hao et al. 2018), both in dense sand. Prototype geometries and important variables are summarised in Table 1, along with tensile capacity $F_y$.

The tests undertaken at the University of Dundee, extensively described in (Davidson et al. 2019) incorporate the installation effect. Three screw anchors were installed in a very dense sand (referred to as VD, $D_r$ = 84% on average) and one in a medium dense sand (MD, $D_r$ = 57%). The tests were undertaken in dry sand at 48g. The stress field generated within the sand box was identical to the effective stress field that would be obtained in a saturated sand at 80g – an approach explained and justified in Li et al. (2010). This approach has previously been validated for lateral pile loading by Klinkvort et al. (2013). The helix diameter $D_h$ of all model anchors installed in very dense sand was equal to 1.7m at prototype scale (scaling factor equal to 80g). Two of these models (U1VD-A and U1VD-B) had a single helix while the third one (U2VD) possessed two helices whose spacing was equal to 2 helix diameters. The helix diameter of the model (U1MD) installed in medium-dense sand was equal to 3.4m. The core diameter $D_c$ was equal to 0.88m for very dense sand models and 1.13m for the medium-dense sand. The helix pitch was constant and equal to 0.56m. All models were installed at a constant rotation rate equal to 3RPM. The advancement rate was chosen to equal one helix pitch per revolution to limit disturbance, i.e. pitch-matched installation as recommended in the literature (Perko 2000). The vertical load or crowd force ($F_{y,min}$) required to maintain the prescribed penetration rate of the model was recorded during the test. The installation process and the uplift loading in both centrifuge tests and numerical simulations were imposed sufficiently slow to represent drained installation and loading conditions, representative of the offshore conditions. The tests were also modelled dry to assure this was the case as mentioned previously.

The second set of data used for independent validation consists of tests published by Hao et al. (2018). These tests consist of flat plate and helical plate anchors (0.4m diameter) were placed into a strongbox and the sand was pluviated all around them, before each anchor was tested in tension. In this case, there is no installation effect and the model anchors can be considered as experimentally wished-in-place. The target global density of the different samples ranged between 85% and 96% and the samples were spun at 20g. The helix diameter $D_h$ at the prototype scale was equal to 0.4m while the core diameter $D_c$ was equal to 0.094m. The helix pitch was constant and equal to 0.1m at prototype scale.

General scaling laws and practical recommendations were respected to ensure the similitude of centrifuge tests at prototype scale (Garnier et al. 2007). The diameter of the smallest helix/plate ($D_h$) to the mean grain size ($d_{50}$) considered here exceeds 150. If it is assumed that helix behaviour is controlled by shear band propagation, this value must exceed the range of 50 to 100 recommended in Garnier et al. (2007). Additionally, this also exceeds the recommendations in for grain size effects on pull out of anchors reported by Garnier et al. (2007) of plate width, B ratio to $d_{50}$ of greater than 48. In addition, the helix pitch to $d_{50}$ ratio was larger than 50, which was assumed adequate to allow the movement of all particles throughout the helix during the installation process. Studies based upon Discrete Element modelling (DEM) with far fewer particles actually modelled between the helix plates showed good correlations with centrifuge testing (Sharif et al. 2019). The smallest pile shaft diameter gave a minimum value of $79d_{50}$ satisfying the lower bound recommendation in Garnier et al. (2007) of 50 times $d_{50}$ regarding the ratio of pile to average grain size diameter.

*Geometry of the numerical model*

In terms of screw pile geometry it is common to idealise the helices as horizontal plates connected to the pile core at a depth representative of the mid pitch of the true helix (Livneh and El Naggar 2008; Al-Baghdadi 2018; Pérez et al. 2018). This hypothesis has been tested through centrifuge experiments on wished-in-place (WIP) screw anchors by Hao et al. (2018), who showed that the uplift capacity of flat and helical plates was almost identical. A similar result was found numerically for WIP anchors by (Al-Baghdadi 2018). This simplification allows screw anchors to be modelled under axisymmetric conditions due to the symmetry of the geometry and loading (in tension or compression). The anchor elements were here modelled using 5-node plate elements based on Reissner-Mindlin's theory (Zienkiewicz and Taylor 2000). The properties of the plates, matching the centrifuge models, are reported in Table 2. The anchor and helix structural behaviour was assumed to be purely elastic. Elastic structural response was observed for all centrifuge test cases considered and would be desirable in design. The thickness of the plate and helix used at UWA was not specified, therefore they were assumed very stiff and the same helix/plate properties were used for all tests.

The soil was modelled by 15-node triangular 2D axisymmetric elements. The mesh was chosen to be a good compromise between accuracy of results and CPU time required for simulations. It was different for each geometry, but all meshes were refined close to the helices and in a zone extending to $3.5D_h$ from the anchor core so that failure surface could be modelled with enough precision. The boundary conditions were representative of the centrifuge tests in each case and were sufficiently spaced from the screw anchors to avoid any interference. The bottom boundary lies $7D_h$/$10D_h$ below the helix while the lateral boundary was located $17D_h$/$30D_h$ from the core for UoD and UWA tests respectively. The displacement was fully fixed along the bottom boundary and normally fixed (i.e. allowing vertical displacement) along the vertical boundaries. The numbers of elements used for each screw anchor mesh are reported in Table 3. A force (for load-controlled stages during installation modelling) or displacement (for displacement-controlled virtual load test) was applied at the top of the shaft to be consistent with the centrifuge experiments.

Zero-thickness 5-node interface elements were used to simulate the interactions between the helix/core and the soil or shear bands within the soil (see later). They were defined on each side of the plate elements. These interface elements allow the opening of a gap between plate and soil when the contact stresses reduce to zero, as well as tangential sliding after friction mobilisation.

*Soil constitutive model*

The 'hardening soil model with small strain stiffness' (HSsmall) was adopted to simulate the sand behaviour (Schanz 1998; Schanz et al. 1999b; PLAXIS 2017b). The parameters of the HST95 Congleton sand, used for the centrifuge tests at the UoD, have been calibrated previously against laboratory element tests as described elsewhere (Lauder et al. 2013; Al-Defae et al. 2013). The use of this model has been comprehensively validated against 1-g, centrifuge and field tests, encompassing various boundary value problems, including piles (e.g. Al-Defae *et al.* 2013; Knappett *et al.* 2016; Al-Baghdadi *et al.* 2017).

The constitutive model is composed of a shear-strain hardening yield surface. It assumes that the stress and strain describe a hyperbolic relationship for the primary triaxial loading of a soil sample and the yield surface converges towards the Mohr-Coulomb surface. It encompasses a tension cut-off to prevent tension loading of the soil and a second volumetric strain hardening yield surface to reproduce oedometric stress paths. The model stiffness is confinement dependent and secant stiffness degrades as shear strain increases. The unloading/reloading elastic stiffness is not a function of the shear strain. The volumetric behaviour is non-associated and is related to the dilatancy angle as reported elsewhere (PLAXIS 2017b). It includes a dilatancy cut-off, ensuring the current void ratio remains lower or equal to the maximum void ratio. All parameters used for the very-dense and medium-dense models are reported in Table 4. They were previously determined for a large range of relative densities based on shearbox and oedometer tests by Al-Defae *et al.* (2013) and were subsequently further validated against drained triaxial compression tests.

The UWA samples were prepared in a dry fine to medium sub-angular silica sand, at relative densities ranging from 85% to 96%. There is no published triaxial data to calibrate the HSsmall model parameters, only the critical state friction angle $\phi'_{cv}\ (=31°)$ was provided in the paper and the authors assumed that the peak friction angle $\phi'_{pk}$ could be calculated according to

$$\phi'_{\mathrm{pk}} = \phi'_{cv} + m_{tr}\, I_R \tag{2}$$

where $I_R$ is the relative dilatancy angle and $m_{tr} = 3$ for triaxial conditions are obtained from (Bolton 1986).

$$I_R = 5D_r - 1. \tag{3}$$

The resulting peak friction angles range from 41.2° to 42.4° respectively. The dilatancy angle was selected to be consistent with the formulation of the hardening soil model (Schanz and Vermeer 1996)

$$\sin\psi'_{pk} = \frac{\sin\phi'_{pk} - \sin\phi'_{cv}}{1 - \sin\phi'_{pk}\sin\phi'_{cv}} \tag{4}$$

for which the dilatancy index ranges from 12.3° to 14.1°. The buoyant unit weight varies between 10.5 and 10.6kN/m³. The rest of the parameters, especially stiffness parameters, are assumed to be identical to the HST95 sand parameters and are defined as a function of the relative density in Table 4.

The interface behaviour was also described by the HSsmall model. For the soil-steel interface elements, the friction and dilatancy angle were defined equal to 27° and 0° respectively, (Lauder et al. 2013). The dilatancy angle of the soil-soil interface at the critical state was set equal to zero while it remained equal to the peak value otherwise. The soil was assumed completely saturated (with a fully drained response) and the water level was located at the soil surface.

*Modelling methodology*

The methodology developed to capture both a consistent anchor capacity and stiffness is described here and summarised in Figure 2. The methodology is based on two successive numerical simulations of increasing complexity (stages 1 and 2), with output from the first stage informing the second. This multi-stage approach allows for the effects of installation-induced soil stress distribution disturbance to be modelled in a self-contained and approximate way, without requiring centrifuge or field load test data to back-calculate appropriate soil parameters in disturbed soil, and is therefore a significant improvement for practical application compared to the recent method of Perez et al. (2018). It is based only on known geometrical parameters of the screw anchor, the in-situ relative density, which in sands can be used to determine the required soil parameters (Table 4), and the measured crowd force during installation. This final parameter can be predicted using the CPT-based relationships presented by Davidson et al. (2018), and can subsequently be refined using measurements from the installation rig in the field or on the centrifuge. However, this procedure does not reproduce the soil displacement due to the shaft penetration and helix movement. The extrapolation of the results to geometries inducing significantly larger or lower shaft diameters should thn be done cautiously.

The stage 1 simulations (Figure 2(a)) were based on the minimal number of hypotheses and composed of three distinct phases. Firstly, the geostatic stress field distribution was initialised within the soil. The initial distribution of the horizontal stresses was based on the Jaky formula (Jaky 1944) and the screw anchor is considered to be wished-in-place at a depth corresponding to each test. Secondly, the compression load corresponding to the recorded installation crowd force at the final helix depth was applied under load control, then reduced to zero (simulating removal of the installation rig). Finally, a vertical upward displacement was imposed at the top of the core to simulate the uplift. The numerical simulations were stopped when the ultimate capacity was reached which corresponds to vertical displacements ranging from 0.1 to $0.3D_h$. Failure of the anchor corresponds to a peak or plateau in the load-displacement relationship and the formation of an uplift failure mechanism, as reported in Figure 2(a).

In stage 2, the numerical model was enhanced to improve the prediction of both anchor capacity and initial stiffness. To improve the capacity prediction (Figure 2(b)), discrete soil-soil interface elements, oriented along the shear plane locations identified from stage 1, were introduced in the mesh, as shown in Figure 2(b). Reduced strength parameters, corresponding to localised soil softening, were defined over a limited zone, based on the analysis of the magnitudes of the shear strains, as shown in Figure 2(b). This analysis is made by inspection of shear strain contour plots at failure (peak or plateau in the load-displacement relationship) from stage 1 simulations. It can be assumed that the soil will enter the post-peak softening regime for shear strain larger than a given threshold. This variable can be obtained from experiments, e.g. as the stain at which critical state strength is achieved from a direct shear test. For the HST95 sand, it is approximately 7.5% as in (Al-Defae et al. 2013), or approximately 15% from triaxial tests (Robinson 2016). For the cases presented herein, this threshold strain was assumed equal to be 10% for the HST95 sand used by Davidson et al. (2019) and it was assumed identical for application to the results of (Hao et al. 2018) as no specific element test results for this case were available. The distance over which a shear strength corresponding to the critical state parameter can then be identified by inspection of the shear strain contour in the FE software. The corresponding interface properties are then assigned to two different zones, corresponding to the softening and peak states.

This approach can be defined as a hybrid FE-Limit Analysis and has several advantages for practical design. It incorporates the effect of soil volumetric compression on the failure mechanism, unlike Limit Analysis (as reported in Cerfontaine et al. 2019). In addition, the approach does not require complex numerical solutions to avoid problems resulting from the use of strain-softening models (Anastasopoulos et al. 2007). Indeed, real shear bands have the width of several sand grains (5 to 40$d_{50}$, where $d_{50}$ is mean particle size of the sand (Desrues and Viggiani 2004; Lauder et al. 2012)), which reduces almost to a zero-thickness interface at the scale of a boundary value problem. The rigorous simulation of such shear bands would require an extremely fine mesh (size equal to approximatively 3$d_{50}$; Gudehus and Nübel 2004) or regularisation techniques introducing some mesh-size dependence, (e.g. Anastasopoulos et al. 2007).

Also, in stage 2 (Figure 2(c)), the stiffness prediction was improved by considering the stress field modification around the anchor due to the varying crowd force applied during its installation. Indeed, this force induces settlement and generates soil hardening over a zone which is several helix diameters wide around the anchor. This installation effect is approximated by simulating several loading/unloading phases, as depicted in Figure 2(c), where the compression force applied corresponds to the position of the helix at a given depth. This loading/unloading is applied at five successive depths to simulate the installation process. Only the structural elements of the screw anchors above this depth are activated, which is similar to the press-replace method developed for displacement piles (Engin et al. 2015), where soil elements are progressively replaced by pile elements to simulate its installation. The compressive stress bulb beneath a helix plate extended to approximately 4$D_h$ below it. Therefore, it was decided to apply a compression step every 1.5$D_h$, to ensure the soil would be relatively uniformly preloaded, while maintaining the complexity of the mesh and computational time to a reasonable level. This distance is lower than the limit for helix interaction in compression, equal to 2$D_h$ (Al-Baghdadi 2018). A simulation based on 7 installation steps did not show any difference in the load-displacement relationship. The crowd forces applied in these phases can be either predicted by the CPT method proposed in (Davidson et al. 2018) or values from the installation rig.

*Mesh influence*

Five different meshes with increasing number of elements were considered, to assess the influence of the mesh size on the results of the stage 1 simulations. The overall number of elements was set up by the user and the size of elements automatically adapted by the software. The initial stiffness and hardening phases were very similar for the different number of elements. Therefore, only the capacity at 0.1$D_h$ and at peak were compared. Results are reported in Table 5 and show that the peak capacity increases with the number of elements and mesh refinement, although this increase is very small between meshes #4 and #5. The simulation related to the mesh 1 stopped converging before the endf the simulation. The inspection of the shear strain field show that the shear band is narrower and more marked as the mesh refinement increases, as would be expected. The overall variability of the anchor capacity is limited, especially with respect to the variability that could be expected for real case studies. The choice of a mesh was then based on the CPU time required to obtain simulation results. The mesh #4 (3175 elements) was adopted as a good balance between mesh refinement and calculation time.

## VALIDATION AGAINST CENTRIFUGE TESTS

This section compares the numerical simulations with the centrifuge tests. The key variables (stress and strain fields) are analysed to illustrate how the methodology was developed and explain how it affects the final results.

### *Wished-in-place anchors (UWA)*

The enhancement of the capacity was validated first against wished-in-place tests of UWA. The two-stage procedure was applied, but only the capacity was enhanced, as there was no installation effect to take into consideration. The extent of the failure mechanism was inspected in results from stage 1 and the softening zone was applied along the interface elements in stage 2. In this case, this zone was around $2.5D_h$ in length. An example of the load-displacement relationship is illustrated in Figure 3 and shows that the stiffness and capacity are relatively consistent with the Stage 2 simulations, while Stage 1 overpredicts the capacity. The peak capacity was identified for 5 different relative embedment ratios and compared in Figure 4 with centrifuge test reported by Hao et al. (2018). Results at shallow embedment ratios ($\leq$ 9) are relatively consistent with the experimental results, particularly given the greater uncertainty in the selection of some specific soil parameters in these cases. The simulations at the largest relative embedment ratio overpredict the capacity, but a deep failure mechanism (e.g. Meyerhof and Adams (1968)) has clearly been reached in the centrifuge testing, which is out of scope of this study.

### *Anchors installed in-flight (UoD)*

Figure 5 compares the measured prototype centrifuge uplift load with the total vertical reaction load at the top of the anchor shaft, $F_y$, obtained from the numerical simulations: purely wished-in-place (stage 1), enhanced capacity only (stage 2 – capacity) and full methodology (stage 2 – capacity/stiffness). All results are depicted as a function of the normalised vertical displacement $u_y/D_h$.

The initial stiffness of wished-in-place simulations (Stage 1) was relatively well captured by the different simulations although the different curves diverged rapidly (at approximately $u_y/D_h$ =0.01) for the two single helix anchors embedded in very dense sand, as shown in Figure 5 (a, c). However, the maximum loads obtained numerically, corresponding to a fully formed failure mechanism, overpredicted the centrifuge test results in each case, from +25% (U1VD-A) to +43% (U1VD-B). They also overestimated the vertical displacement required to reach this maximum capacity, which was equal to 0.1Dh for the centrifuge tests and close to 0.25Dh for numerical simulations.

The enhanced capacity simulations (stage 2 – capacity), incorporating soil-soil interface elements based on stage 1 results, show that the prediction of the uplift capacity was considerably improved for single helix anchors (Figure 5 (a, c)), although the prediction for the double helix case was strongly degraded (Figure 5 (d)). However, the initial stiffness was underpredicted in very dense sand. Detailed discussion of the parameterisation of the soil-soil interface elements resulting in the curves shown in Figure 3 is presented in the following Discussion section.

Results of the simulations incorporating installation effects (stage 2 – capacity/stiffness) were the most consistent with the centrifuge tests, as depicted in Figure 5. The load-displacement relationship and initial stiffness were more consistent with the centrifuge tests for both single helix anchors embedded in very dense sand compared to previous predictions, as shown in Figure 5 (a, c). The initial stiffness was slightly overpredicted in the medium dense case (Figure 5 (b)). The difference was more pronounced in the double helix case (Figure 5 (d)) and the initial stiffness was almost identical for all three very dense simulations.

The difference between all those simulations can be explained through the inspection of the failure mechanism (capacity) and stress distribution (stiffness) around the anchor before and at failure. This analysis is undertaken in the following. In addition, the procedure to inspect Stage 1 results to derive Stage 2 simulations is detailed.

## DISCUSSION

### *Failure mechanisms*

Five distinct variables were considered to identify and interpret the uplift failure mechanism for the wished-in-place (Stage 1) simulations. Two of these variables were cumulative over the simulation, namely the vertical displacement $u_y$ and shear strain $\gamma_s$, and were therefore influenced by the complete deformation history of the screw anchor. The three other variables were instantaneous for a given load step, namely the increments of vertical displacement $\Delta u_y$ and shear strain $\Delta\gamma_s$, and the current plastic points (PP, i.e. integration point reaching the plastic yield surface). These variables have been used previously to interpret the failure mechanism of plate anchors embedded in sand (Cerfontaine et al. 2019) and are depicted in Figure 6 for the single deep helix anchor embedded in very dense sand (U1VD-B) as an example. The results show the progressive formation of the failure mechanism, which had not been constrained by soil-soil interface elements at this stage.

Figure 6(a) describes the state of the soil after applying the (maximum, last recorded) crowd force at the end of installation and unloading to zero compression. It indicates that shear bands pointing towards the developed during the first phase were reactivated (in the opposite direction) during uplift. After 0.1-0.2$D_h$ imposed uplift displacement, the failure mechanism was not fully formed as shown in Figure 6(b and c). Several shear bands seemed to initiate from the helix edge at different orientations. The failure mechanism observed in this study was fully formed after a displacement equal to $0.3D_h$ and corresponded to a shallow wedge of soil (i.e. shallow failure mechanism).

The conical shape of this shallow failure mechanism is consistent with previous experimental studies undertaken for buried anchors (e.g. Ilamparuthi and Muthukrishnaiah 1999; Liu *et al.* 2012) where image analysis of the failure mechanism through a Perspex face was undertaken and analytical approaches (e.g. Das and Shukla 2013). However, the exact inclination of this conical mechanism previously reported varied from study-to-study, as described in Cerfontaine et al. (2019) for plate anchors. For the screw anchors considered here, the failure mechanism diverged slightly from a straight line and its orientation was close to the assumed mechanism from Giampa *et al.* (2017), i.e. inclined at the dilatancy angle ($\psi'_{pk}$ =17° for the very dense sand, indicated by a dashed line in Figure 6) to the vertical direction. This inclination appears consistent with previous theoretical analyses for shallow anchors (Vermeer and Sutjiadi 1985) and experimental evidence for uplifting pipelines (White et al. 2008). Similar conclusions were drawn from interpretation of the medium-dense sand results (not shown). It is noted though that these additional studies do not include installation effects, but still provide some insights into potential failure mechanisms that may be expected in uplift. It is also noted that specific effects of soil density changes due to installation and their subsequent potential effects on the nature of the failure mechanism may not be fully captured in these studies.

The failure mechanism of multi-helix anchors depends on the inter-helix spacing. If two adjacent helices of identical diameter are sufficiently close, a cylindrical failure surface, whose diameter is equal to the helix diameter, is assumed to form between them in tension or compression (Tsuha et al. 2007; 2012; Knappett et al. 2014; Al-Baghdadi et al. 2017a). At greater spacing, the helices may act independently. The evolution of the failure mechanism is depicted in Figure/span>7 at different time steps for the double helix case (U2VD). The failure mechanism occurred for a lower imposed vertical displacement ($0.1D_h$) than the single helix case. It consisted of an inter-helix failure plane and a shallow wedge mechanism, which was oriented along the proposed failure mechanism of Giampa et al. (2017). Figure 7(b-c) show that there was a competition between several shear bands during the uplift of the screw anchor. Additional shear bands were initiated at the edge of the bottom helix or at a position in between the two helices, but they did not reach the surface. In summary, it is clear that for a multi-helix anchor, the embedment depth of the upper helix plate appears to control the apparent wedge-shaped uplift mechanism observed in this study and that at lower displacements there is fluctuation between a cylindrical mechanism and wedging emanating from the lower helix.

The inspection of results presented in Figure 6 and Figure 7 was used to define the soil-soil interface geometry of stage 2 (enhanced capacity). This allowed the modelling of a greater slip deformation at failure without excessive mesh distortion and to allow strain-dependent softening (at failure) to be incorporated. For single helix anchors, the soil-soil interface elements were inclined at the dilatancy angle to the vertical direction as per (Giampa et al. 2017) (shallow wedge). For the double helix case, the interface was set-up similarly from the upper helix, while a cylindrical failure mechanism (vertical interface elements) was enforced between the lower and upper helices.

Figure 6 shows that large shear strain developed along the failure mechanism in stage 1. It was greater than 30% close to the anchor edge and decreased up to a normalised distance along the failure mechanism $\xi/D_h$ of approximately 2. The distribution then decreased almost linearly up to the surface. Results of experimental triaxial tests (Robinson 2016) as well as direct shear tests reported by Al-Defae et al. (2013) suggest that HST95 sand appears to soften at shear strains greater than 2-3% for medium-dense to dense sand. A larger shear strain is necessary (>10%) before reaching the critical state, depending on the soil density and confinement. Consequently, soil-soil interface properties in the zone closest to the anchor, namely the softening zone, considered that critical state strength was mobilised within the interface after peak. The length of this softened zone was based on the analysis of shear strain contour results from the stage 1 analysis (rather than by back-fitting empirically to match the centrifuge measured capacity). This was approximately $2D_h$ for screw anchors in very dense sand and $2.5D_h$ in medium dense sand. Beyond this zone, the interface properties were identical to the virgin soil properties. It is verified that the pre-definition of a failure-mechanism does not create a new global failure pattern. This is shown in Figure 8 for the single helix case (U1VD-B), where the plastic points, shear strain and vertical displacement all described a wedge failure mechanism whose shape is identical to the pre-defined one.

*Stress distribution along the failure mechanism*

Most analytical approaches to screw anchor design consider that failure in uplift occurs between rigid soil blocks and assumes a normal shear stress distribution, based on peak friction angle, increasing linearly with depth (Ghaly et al. 1991b; Giampa et al. 2017). However, the soil is far from rigid and significant vertical displacement was required to fully mobilise the failure mechanism, as shown in Figure 5. Subsequently, the load applied by the helix on the soil generated vertical strain. Lateral strain was constrained by the surrounding soil, increasing the lateral stress distribution, as shown numerically by Cerfontaine et al. (2019) for plate anchors or experimentally for screw piles in a pressure chamber (Nagata and Hirata 2005; Nagai et al. 2018). The stress distributions around the anchor and along the slip surface were then modified, such that the normal and shear stresses at failure were increased. Figure 9 (a and b) show the normal and shear stress distributions along the slip surface (inclined at $\theta$ =17° to the vertical) for the single helix anchor in very dense sand (U1VD-B) for the wished-in-place (Stage 1) simulation. The results are plotted as a function of the normalised distance $\xi/D_h$ from the edge of the helix, in the direction of the slip surface. The results are normalised with respect to the maximum normal and shear stresses assumed in the approach proposed by (Giampa et al. 2018b) since their failure mechanism is identical to the one observed in this study, where:

$$\tau_{G,max} = \tan \phi'_{pk} \sigma'_{N,G,max} = \tan \phi'_{pk} \cos\left(\phi'_{pk} - \psi'_{pk}\right) \gamma' H \quad (5)$$

From in Figure 9 (a and b) the maximum values measured were several times those assumed in the (Giampa et al. 2018b) approach (which assumes a rigid block of soil), even after small vertical displacements.

The stress distribution along the interface is compared for both stages 1 and 2 in Figure 10. Results show that both normal and shear stress distributions are modified (reduced in magnitude) in the softening zone. However, the decrease is more significant for the shear stresses as they are both (i) proportional to the reduced normal effective stresses and (ii) the friction angle is reduced to critical state. Finally, both stress distributions are significantly different from the linear distribution assumed by Giampa et al. (2017, 2018b) (even if the uplift capacity is well approximated) or any other analytical methods. This indicates that the FE method may be preferable to analytical methods, even if only capacity is of interest.

*Depth and density effect*

Additional simulations for relative embedment ranging between $1 \leq H/D_h \leq 8$ for relative densities between 57-84% were conducted to increase the generality of previous observations. Cross-sections along failure planes inclined at the dilatancy angle to the vertical (dilatancy angle is a function of relative density) at each embedment ratio are compared in Figure 11 for $D_r$ = 84% (as an example). Figure 11(a-b) show that the maximum normal and shear stress at failure increase with depth, which is consistent with observations made by Cerfontaine et al. (2019) for plate anchors.

The length of the shear band where high shear strain occurs was assessed through a systematic analysis of the shear strain output (cross-sectional strain contour plot such as Figure 6) at failure. A threshold of shear strain above which strain-softening was expected to develop was established, equal to 10% for all simulations and corresponding to the shear strain required to reach the critical state at these densities. The equivalent length of the assumed failure mechanism along which softening occurred is shown in Figure 12. This figure shows that the length of the softening zone was almost equal to zero at $H/D_h$=1 and increased linearly up to a certain depth ($H/D_h$ = 3 and 4 for very dense and medium dense sand respectively). Above these normalised depths, the softening zone length appeared to be constant, although some scatter was observed.

The procedure (addition of soil-soil interface elements) was applied to a single helix screw anchor embedded in both sand densities for a varying embedment ratio. The length of the softening zone was based on results presented in Figure 12. Results in Figure 13 show that the stage 2 simulations generate a significant decrease in bearing capacity. A comparison with the uplift capacity obtained through the approach of Giampa *et al.* (2017) shows that it is consistent with the numerical results, even at larger relative embedment ratios, for a $D_r$ = 84%, although it should be noted that the postulated stress distribution in that method is different.

*Installation effect*

The installation procedure mainly affected the stiffness for single plate screw anchors, rather than the capacity, as shown in Figure 5 by comparing the two stage 2 FE curves. In addition, Table 6 shows that the magnitude of the compression load has a limited impact on the ultimate uplift capacity for the single helix screw anchor. An increase or decrease of the crowd force by 50% over the whole installation process, generates only a variation of 7% in the uplift capacity. However, the stiffness is affected by this crowd force magnitude. This can be mechanically explained through the analysis of the unloading/reloading Young modulus $E_{UR}$ and the average stress fields induced around the anchor just before uplifting which are shown in Figure 14.

The large compression (crowd) force applied during installation had several consequences. Firstly, the soil was sheared over a zone of soil that was several helix diameters in size. As the soil was strained, its secant stiffness decreased (beyond the range of small-strain stiffness). After the soil was loaded in compression up to a deviatoric stress $q_{comp}$ (as shown in Figure 15(a)), the yield surface hardened, and its unloading stiffness was based on the $E_{UR}$ modulus. Consequently, the reloading of the soil during the uplift phase will follow the same path up to $q_{comp}$ and will be much stiffer than a stress-strain path starting at the origin of the axes.

Secondly, the stress field around the anchor was modified by the compressive crowd load, as can be observed in Figure 14(c, d). Consequently, the strength and stiffness increased, as they were a function of the average stress, as illustrated in Figure 11(b) and in the following evolution of the unloading/reloading modulus $E_{ur}$ definition

$$\mathrm{E_{ur}}(p') = E_{ur}^{ref}\left(\frac{p'}{p'_{ref}}\right)^{m} \tag{6}$$

where $E_{ur}^{ref}$ is the reference modulus for $p'_{ref} = 100kPa$, *p'* is the average stress and *m* is a material parameter. The consequence of these combined effects is a very complex pattern of operative stiffness all around the anchor prior to uplift, as depicted in Figure 14(a, b). However, it is clear that the stiffness above the anchor, in a zone delimited by the expected failure mechanism (dashed line), was larger if the entire installation process was accounted for (stage 2), rather than only the last recorded compression load (stage 1).

It should be noted that the installation simulation did not modify the shape of the failure mechanism. Additional uplift simulations were run, incorporating the installation simulation, but with no pre-defined mechanism. The observed failure mechanism was identical to that from the stage 1 simulation.

*Cylindrical failure mechanism*

Schiavon (2016) and Perez et al. (2018) recently investigated the disturbance effect around screw anchors in centrifuge tests. The authors carried out micro-tomographic analyses of the sand around the screw anchor and identified that the vertical soil column above the helix was highly disturbed (lower density). They concluded that the failure mechanism should be a vertical cylindrical failure whose section is identical to the area of the helix. This result is consistent with experiments undertaken in calibration chambers (Nagata and Hirata 2005; Nagai et al. 2018), which exhibit a cylindrical failure mechanism, although the pressurised calibration chamber process impedes the development of any shallow failure mechanism. To replicate this mechanism, Perez et al. (2018) introduced two cylindrical zones of soil in their finite element simulations, whose properties where back-calculated to reproduce the centrifuge tests. The friction angles leading to the best fit of the experimental results were close to the critical state friction angle.

The cylindrical failure mechanism hypothesis has been tested in the following with or without an installation process. Three scenarios incorporating a pre-defined cylindrical failure mechanism, were compared with reference simulations for the U1VD-A case in Figure 16. The first simulation included a cylindrical failure mechanism using a reduced friction angle ($\phi_r = 40°$), lying between the undisturbed peak and the critical state friction angle. Results show that the load-displacement relationship was similar to the stage 1 simulation where there is no pre-defined failure mechanism at all. This was corroborated by the inspection of the failure mechanism (shear strain), which showed a conical pattern as before.

Two other simulations adopted the same cylindrical failure mechanism as per micro-tomographic observations of Schiavon (2016) but used the critical state friction angle along the cylindrical failure mechanism, which would be consistent with a highly disturbed zone of soil. In this case, modelling the crowd-force installation effects, i.e. combining density and stress installation disturbance, makes a significant difference to the capacity obtained (Figure 16, with installation, 1MN, without, 5MN), but the maximum capacity is still lower than both the reference simulation and the centrifuge results.

In summary, the centrifuge results obtained at the University of Dundee and presented in (Davidson et al. 2019) are better approximated by a conical shallow failure mechanism while a cylindrical failure mechanism gives a better approximation of the results for the numerical simulations of Pérez et al. (2018). These two possibilities are not necessarily mutually exclusive. Large geometries representative of the offshore requirements were used in this study while Pérez et al. (2018) presented results for typical onshore piles, which are much smaller. This difference in scale and in geometry ($D_h/D_c$ ratio, tip shape) can lead to different stress distribution or disturbance around the anchor and generate different failure mechanism. In any case, the principal benefit of the new two-stage approach over that proposed by Perez et al. (2018) is that there is no need to assume a priori empirically-derived strength reduction factors as the final simulation is informed by directly measured soil parameters, the results of the stage 1 WIP simulation and an explicit (though approximate) simulation of the installation process. Further research is necessary to improve the methodology proposed here, for instance by incorporating density variations resulting from the installation process, i.e. the shaft and helix penetration.

*Application in engineering design*

The two-stage simulation process presented herein can in principle be applied to any soil profile and can provide the full load-displacement curve, allowing both uplift capacity and stiffness at working load to be assessed. The process can be summarised by the following steps:

1. Determine the crowd force required to install the screw anchor as a function of depth, using a methodology previously developed (Davidson et al. 2018);
2. Conduct an uplift simulation (stage 1) of the screw anchor in the 'wished-in-place' configuration;
3. Assess the shear band pattern from stage 1 output and the distance over which softening should take place based on the induced shear stresses, with respect to laboratory test results for the soil in question (e.g. direct shear test);
4. Modify the stage 1 model (from (2)) to include a multi-step press-replace procedure (informed by predicted crowd forces from (1)) followed by the addition of soil-soil interfaces with appropriate softening behaviour at the location of the shear bands (from (3)) to the final (installed) anchor configuration;
5. Run the stage 2 model to determine the anchor performance (load-displacement relationship).

It should be noted that this procedure has only been validated here for large dimension screw anchors (representative of offshore applications) embedded in uniform deposits of sand at a relatively shallow depth ($H/D_h \leq 8$). In such deposits, as a first approximation, the process might be shortened by defining directly the failure mechanism as a shallow wedge whose inclination to the vertical is equal to the dilatancy angle and defining the reduced strength distance for the soil-soil interface based on Figure 15. This would have the effect of removing stage 1. If the uplift capacity only is required (e.g. in initial Front-End Engineering Design), the step preloading phase might also be neglected as a first approximation for single helix anchors.

## CONCLUSION

In this paper, a numerical methodology, based on the Finite Element (FE) method, has been derived to enable predictions of the entire load-displacement relationship (including the stiffness at working load and uplift capacity) of screw anchors embedded in sand. It meets a need to provide improved prediction of uplift capacity (which is significantly overestimated using existing analytical methods) identified from the literature, which is required for anchor sizing, and additionally provides information on (non-linear) anchor axial stiffness which controls the global rotational deformation of a jacket structure or tension-leg platforms. This methodology is applicable in principle to any screw anchor geometry and ground conditions and can be fully parametrised based on basic soil element testing and in-situ (CPT) tests in sands. Installation-induced initial conditions within the soil can be approximated using predicted crowd forces, based either on CPT data using a previously developed prediction method, or from crowd force measurements taken from the installation records in the field.

The predictions of screw anchor tensile uplift performance were consistent with centrifuge test results, with or without installation effects, that were previously published in the literature. The FE analyses revealed that, as a significant vertical displacement is required to fully form the failure mechanism, high induced shear strain along a part of the failure mechanism close to the helix is such that critical state should be reached. The numerical results also showed that the compression (crowd) load applied during the screw anchor installation phase modifies the stress field around the anchor, which in turn affects the anchor uplift stiffness.

The methodology developed in this paper, enables the prediction of uplift capacity (ultimate limit state) and stiffness (serviceability limit state), accounting for installation effects in an approximate way without empirical modifications to soil properties, and so can be used to assess screw anchor performance using commercially available FE software. This approach could lead to cost reduction, more reliable and efficient screw anchor design, enabling the generalisation of this anchorage solution for applications in offshore geotechnical engineering.

## ACKNOWLEDGEMENTS

This project has received funding from the European Union's Horizon 2020 research and innovation programme under the Marie Skłodowska-Curie grant agreement No 753156. The authors would like to acknowledge the support of the Engineering and Physical Science Research Council (EPSRC) (Grant no. EP/N006054/1: Supergen Wind Hub Grand Challenges Project: Screw piles for wind energy foundations). The 5th author would like to acknowledge the financial support of the Iraqi Ministry of higher Education of Scientific Research (MOHESR). Elements of this work were undertaken using facilities developed as part of the ERDF-funded Scottish Marine & Renewables Test Centre (SMART) at the University of Dundee.

## SYMBOLS

| | |
|---|---|
| $A$ | Helix area (including core area) |
| $d_{50}$ | Is the size of particles such that 50% of the particles are smaller than this size. |
| $D_c$ | Core diameter |
| $D_h$ | Helix diameter |
| $D_r$ | Relative density |
| $E_{ur}, E_{ur}^{ref}$ | Unloading/reloading Young modulus and reference Young modulus respectively |
| FE | Finite element |
| $F_y$ | Vertical load applied at the top of the screw anchor (positive in tension) |
| $H$ | Helix embedment depth |
| $I_R$ | Relative dilatancy index, (Bolton 1986) |
| $m$ | Material parameter of the HSsmall model |
| MD | Medium-dense sand ($D_r$ =57%, UoD test) |
| $N_\gamma$ | Non-dimensional uplift bearing factor |
| $p'$ | Average stress |

| | |
|---|---|
| $p'_{ref}$ | Reference pressure for the determination of stress dependent stiffness in the HSsmall model |
| $u_y$ | Vertical displacement measured at the top of the screw anchor |
| VD | Very-dense sand ($D_r$ = 84%, UoD test) |
| $\gamma'$ | Buoyant unit weight |
| $\gamma_s$ | Shear strain |
| $\gamma_{s,th}$ | Threshold of shear strain at which critical state is supposed to be reached |
| $\Delta\gamma_s$ | Increment of shear strain over a time step |
| $\Delta u_y$ | Increment of vertical displacement of a time step |
| $\theta$ | Inclination to the vertical direction of the theoretical straight failure plane emanating from the anchor edge |
| $\xi$ | Normalised distance from the edge of the anchor along the direction of the theoretical straight failure plane |
| $\sigma'_h$ | Horizontal effective stress within the soil |
| $\sigma'_N$ | Normal effective stress along any cross-section within the soil |
| $\sigma'_{N,G}$ | Normal effective stress along the theoretical failure plane according to (Giampa et al. 2017) |
| $\tau$ | Shear stress along any cross-section within the soil |
| $\tau_G$ | Shear stress along the theoretical failure plane according to (Giampa et al. 2017) |
| $\tau_{rel}$ | Mobilised shear stress, ratio of the current to maximum shear stress |
| $\phi'_{cv}$ | Critical state friction angle |
| $\phi'_{pk}$ | Peak friction angle |
| $\phi'_r$ | Residual friction angle |
| $\psi'_{pk}$ | Peak dilation angle |

## REFERENCES


Achmus, M., Kuo, Y.-S.S., and Abdel-Rahman, K. 2009. Behavior of monopile foundations under cyclic lateral load. Computers and Geotechnics, **36**(5): 725–735. doi:10.1016/j.compgeo.2008.12.003.

Al-Baghdadi, T. 2018. Screw piles as offshore foundations : Numerical and physical modelling. PhD Thesis, University of Dundee, UK.

Al-Baghdadi, T.A., Brown, M.J., Knappett, J.A., and Al-Defae, A.H. 2017a. Geotechnical engineering effects of vertical loading on lateral screw pile performance. Proceedings of the Institution of Civil Engineers: Geotechnical Engineering, **170**(3): 259–272. doi:10.1680/jgeen.16.00114.

Al-Baghdadi, T.A., Davidson, C., Brown, M.J., Knappett, J.A., Brennan, A., Augarde, C., Coombs, W., and Wang, L. 2017b. CPT based design procedure for installation torque prediction for screw piles installed in sand. 8th International Conference on Offshore Site Investigation & Geotechnics, (1): 346–353. Society for Underwater Technology, London, UK.

Al-Defae, A.H.H., Caucis, K., and Knappett, J.A.A. 2013. Aftershocks and the whole-life seismic performance of granular slopes. Géotechnique, **63**(14): 1230–1244. Thomas Telford Ltd. doi:10.1680/geot.12.P.149.

Anastasopoulos, I., Gazetas, G., Asce, M., Bransby, M.F., Davies, M.C.R., and Nahas, a El. 2007. Fault Rupture Propagation through Sand : Finite-Element. Journal of Geotechnical and Geoenvironmental Engineering, **133**(August): 943–958. doi:10.1061/(ASCE)1090-0241(2007)133:8(943).

Bachynski, E.E., and Moan, T. 2014. Ringing loads on tension leg platform wind turbines. Ocean Engineering, **84**: 237–248. Elsevier. doi:10.1016/j.oceaneng.2014.04.007.

Bailey, H., Senior, B., Simmons, D., Rusin, J., Picken, G., and Thompson, P.M. 2010. Assessing underwater noise levels during pile-driving at an offshore windfarm and its potential effects on marine mammals. Marine Pollution Bulletin, **60**(6): 888–897. doi:10.1016/j.marpolbul.2010.01.003.

Bolton, M.D. 1986. The strength and dilatancy of sands. Géotechnique, **36**(I): 65–78.

Byrne, B.W., and Houlsby, G.T. 2015. Helical piles: an innovative foundation design option for offshore wind turbines. Philosophical Transactions of the Royal Society A: Mathematical, Physical & Engineering Sciences, **373**(February): 1–11. doi:10.1098/rsta.2014.0081.

Cerfontaine, B., Knappett, J.A., Brown, M.J., and Bradshaw, A.S. 2019. Effect of soil deformability on the failure mechanism of shallow plate or screw anchors in sand. Computers and Geotechnics, **109**(May): 34–45. doi:https://doi.org/10.1016/j.compgeo.2019.01.007.

Das, B.M., and Shukla, S.K. 2013. Earth anchors. J. Ross, Plantation, Florida.

Davidson, C., Al-Baghdadi, T., Brown, M., Brennan, A., Knappett, J., Augarde, C., W., C., Wang, L., Richards, D., Blake, A., and Ball, J. 2018. A modified CPT based installation torque prediction for large screw piles in sand. *In* Cone Penetration Testing. *Edited by* M. Hicks, F. Pisanò, and J. Peuchen. Delft, The Netherlands.

Davidson, C., Brown, M.J., Brennan, A.J., Knappett, J.A., Cerfontaine, B., and Sharif, Y.U. 2019. Physical modelling of screw piles for offshore wind energy. *In* First International Symposium on Screw Piles for Energy Applications. *Edited by* C. Davidson, M.J. Brown, J.A. Knappett, A.J. Brennan, C. Augarde, W. Coombs, L. Wang, D. Richards, D.J. White, and A. Blake. University of Dundee, Dundee, UK.

Davidson, C., Brown, M.J., Cerfontaine, B., Al-Baghdadi, T., Knappett, J., Brennan, A., Augarde, C., Coombs, W., Wang, L., Blake, A., Richards, D., and Ball, J. 2020. Physical modelling to demonstrate the feasibility of screw piles for offshore jacket supported wind energy structures. (submitted for consideration in) Géotechnique,.

Desrues, J., and Viggiani, G. 2004. Strain localization in sand: an overview of the experimental results obtained in Grenoble using stereophotogrammetry. International Journal for Numerical and Analytical Methods in Geomechanics, **28**(4): 279–321. doi:10.1002/nag.338.

Dickin, E.A. 1988. Uplift behaviour of horizontal anchor plates in sand. Journal of Geotechnical and Geoenvironmental Engineering, **114**(11): 1300–1317.

Engin, H.K., Brinkgreve, R.B.J., and van Tol, A.F. 2015. Simplified numerical modelling of pile penetration - the press-replace technique. International Journal for Numerical and Analytical Methods in Geomechanics, **39**(March): 1713–1734. doi:10.1002/nag.2736.

Garnier, J., Gaudin, C., Springman, S.M., Culligan, P.J., Goodings, D., Konig, D., Kutter, B., Phillips, R., Randolph, M.F., Thorel, A., Garnier, J., Gaudin, C., Springman, S.M., Culligan, P.J., Goodings, D., Konig, D., Kutter, B., Phillips, R., Randolph, M.F., and Thorel, L. 2007. Catalogue of scaling laws and similitude questions in geotechnical centrifuge modelling. International Journal of Physical Modelling in Geotechnics, **7**(3): 01–23. doi:10.1680/ijpmg.2007.070301.

Gavin, K., Doherty, P., and Tolooiyan, A. 2014. Field investigation of the axial resistance of helical piles in dense sand. Canadian Geotechnical Journal, **51**(11): 1343–1354. doi:10.1139/cgj-2012-0463.

Ghaly, A., Hanna, A., and Hanna, M. 1991. Uplift behaviour of screw anchor in sand, I dry sand. Journal of Geotechnical Engineering, **117**(5): 773–793.

Giampa, J., Bradshaw, A., and Schneider, J. 2017. Influence of Dilation Angle on Drained Shallow Circular Anchor Uplift Capacity. International Journal of Geomechanics, **17**(2): 4016056. doi:10.1061/(ASCE)GM.1943-5622.0000725.

Giampa, J.R., Bradshaw, A., Gerkus, H., Gilbert, R.B., Gavin, K.G., and Sivakumar, V. 2018a. The effect of shape on the pullout capacity of shallow plate anchors in sand. Géotechnique,.

Giampa, J.R., Bradshaw, A.S., and Schneider, J.A. 2018b. Erratum for "Influence of Dilation Angle on Drained Shallow Circular Anchor Uplift Capacity" by Joseph R. Giampa, Aaron S. Bradshaw, and James A. Schneider. International Journal of Geomechanics, **18**(11): 08218002. doi:10.1061/(asce)gm.1943-5622.0001329.

Gudehus, G., and Nübel, K. 2004. Evolution of shear bands in sand. Géotechnique, **54**(3): 187–201. doi:10.1680/geot.54.3.187.36346.

Hao, D., Wang, D., O'Loughlin, C.D., Gaudin, C., O'Loughlin, C.D.C.D., and Gaudin, C. 2018. Tensile monotonic capacity of helical anchors in sand: interaction between helices. Canadian Geotechnical Journal (in press),. doi:10.1139/cgj-2018-0202.

Houlsby, G.T. 2016. Interactions in offshore foundation design. Géotechnique, **66**(10): 791–825. doi:10.1680/jgeot.15.RL.001.

Ilamparuthi, K., Dickin, E.A., and Muthukrisnaiah, K. 2002. Experimental investigation of the uplift behaviour of circular plate anchors embedded in sand. Canadian Geotechnical Journal, **39**: 648–664. doi:10.1139/t02-005.

Ilamparuthi, K., and Muthukrishnaiah, K. 1999. Anchors in sand bed: Delineation of rupture surface. Ocean Engineering, **26**(12): 1249–1273. doi:10.1016/S0029-8018(98)00034-1.

Jaky, J. 1944. The coefficient of earth pressure at rest. Journal of the Society of Hungarian Architects and Engineers, **78**(5): 355–358.

Klinkvort, R.F., Hededal, O., and Springman, S.M. 2013. Scaling issues in centrifuge modelling of monopiles. International Journal of Physical Modelling in Geotechnics, **13**(2): 38–49. doi:http://dx.doi.org/10.1680/ijpmg.12.00010.

Knappett, J.A., Brown, M.J., Brennan, A.J., and Hamilton, L. 2014. Optimising the compressive behaviour of screw piles in sand for marine renewable energy applications. *In* International Conference on Piling and Deep foundations. Stockholm, Sweden.

Knappett, J.A., Caucis, K., Brown, M.J., Jeffrey, J.R., and Ball, J.D. 2016. CHD pile performance: part II – numerical modelling. Proceedings of the Institution of Civil Engineers - Geotechnical Engineering, **169**(5): 436–454. doi:10.1680/jgeen.15.00132.

Lauder, K.D., Brown, M.J., Bransby, M.F., and Boyes, S. 2013. The influence of incorporating a forecutter on the performance of offshore pipeline ploughs. Applied Ocean Research, **39**: 121–130. Elsevier Ltd. doi:10.1016/j.apor.2012.11.001.

Lauder, K.D., Brown, M.J., Bransby, M.F., and Gooding, S. 2012. Variation of tow force with velocity during offshore ploughing in granular materials. Canadian Geotechnical Journal, **49**(11): 1244–1255. doi:10.1139/t2012-086.

Li, Z., Haigh, S.K., and Bolton, M.D. 2010. Centrifuge modelling of mono-pile under cyclic lateral loads. Proceedings of the 7th International Conference on Physical Modelling in Geotechnics, **2**: 965–970. doi:10.1680/ijpmg.2010.10.2.47.

Liu, J.Y., Liu, M.L., and Zhu, Z.D. 2012. Sand Deformation around an Uplift Plate Anchor. Journal of Geotechnical and Geoenvironmental Engineering, **138**(6): 728–737. doi:Doi 10.1061/(Asce)Gt.1943-5606.0000633.

Livneh, B., and El Naggar, M.H. 2008. Axial testing and numerical modeling of square shaft helical piles under compressive and tensile loading. Canadian Geotechnical Journal, **45**: 1142–1155. doi:10.1139/T08-044.

Meyerhof, G.G., and Adams, J.I. 1968. The ultimate uplift capacity of foundations. Canadian Geotechnical Journal, **5**(4): 225–244.

Mitsch, M.P., and Clemence, S.. 1985. The uplift capacity of helix anchors in sand. *In* Uplift behavior of anchor foundations in soil. Proceedings of the ASCE. New-York, USA. pp. 26–47.

Mosquera, Z.S.Z., Tsuha, H.C., Schiavon, J.A., and Thorel, L. 2015. Discussion of Field investigation of the axial resistance of helical piles in dense sand. Canadian Geotechnical Journal, **52**(11): 1190–1194. doi:10.1139/cgj-2012-0463.

Nagai, H., Tsuchiya, T., and Shimada, M. 2018. Influence of installation method on performance of screwed pile and evaluation of pulling resistance. Soils and Foundations, **58**(2): 355–369. Elsevier B.V. doi:10.1016/j.sandf.2018.02.006.

Nagata, M., and Hirata, H. 2005. Study on Uplift Resistance of Screwed Steel Pile. (92): 73–78.

Newgard, J.T., Schneider, J. a., and Thompson, D.J. 2015. Cyclic response of shallow helical anchors in a medium dense sand. *In* Frontiers in Offshore Geotechnics III. Taylor & Francis Group, London, Oslo, Norway. pp. 913–918.

Papadopoulou, K., Saroglou, H., and Papadopoulos, V. 2014. Finite Element Analyses and Experimental Investigation of Helical Micropiles. Geotechnical and Geological Engineering, **32**(4): 949–963. doi:10.1007/s10706-014-9771-6.

Pérez, Z.A., Schiavon, J.A., Tsuha, C.H.C., Dias, D., and Thorel, L. 2018. Numerical and experimental study on the influence of installation effects on the behaviour of helical anchors in very dense sand. Canadian Geotechnical Journal, **55**(8): 1067–1080. doi:10.1139/cgj-2017-0137.

Perko, H.A. 2000. Energy method for predicting installation torque of helical foundations and anchors. ASCE Geotechnical Special Publication,: 1–11. doi:10.1061/40511(288)24.

Perko, H.A. 2009. Helical Piles: A Practical Guide to Design and Installation. *In* 1st Edit. John Wiley & Sons.

PLAXIS. 2017a. PLAXIS 2D Reference Manual. Delft, The Netherlands.

PLAXIS. 2017b. PLAXIS Material Models Manual. Delft, The Netherlands.

Robinson, S. 2016. Internal report for project Seabed Ploughing : Modelling for Infrastructure EP/M000362/1. Dundee, UK.

Schanz, T. 1998. Zur Modellierung des Mechanischen verhaltens von Reibungsmaterialen. Universität Stuttgart, Germany.

Schanz, T., Vermeer, A., and Bonnier, P. 1999a. The hardening soil model: formulation and verification. *In* Beyond 2000 Comput. Geotech. 10 years PLAXIS. Amsterdam, The Netherlands. pp. 281–296.

Schanz, T., Vermeer, A., and Bonnier, P. 1999b. The hardening soil model: formulation and verification. Beyond 2000 Comput. Geotech. 10 years PLAXIS Int. Proc. Int. Symp. beyond 2000 Comput. Geotech. Amsterdam Netherlands 1820 March 1999,: 281.

Schanz, T., and Vermeer, P.A. 1996. Angles of friction and dilatancy of sand. Géotechnique, **46**(1): 145–151.

Schiavon, J.A. 2016. Comportamento de ancoragens helicoidais submetidas a carregamentos cíclicos. PhD Thesis. University of São Paulo, Brazil.

Sharif, Y.U., Brown, M.J., Ciantia, M.O., Knappett, J.A., Davidson, C., Cerfontaine, B., and Robinson, S. 2019. Numerically modelling the installation and loading of screw piles using DEM. *In* Proceedings of the International Symposium on Screw Piles for Energy Applications. Dundee, UK.

Sutherland, H.B. 1965. Model Studies for Shaft Raising through Cohesionless Soils. *In* Proceedings of the 6th International Conference on Soil Mechanics and Foundation Engineering, Montréal. Montreal, Canada. pp. 410–413.

Tappenden, K.M. 2007. Predicting the axial capacity of screw piles installed in Canadian soils. Msc Thesis, University of Alberta.

Tsuha, C.H.C., Aoki, N., Rault, G., Thorel, L., and Garnier, J. 2007. Physical modelling of helical pile anchors. International Journal of Physical Modelling in Geotechnics, **494**(4): 1–12.

Tsuha, C.H.C., Aoki, N., Rault, G., Thorel, L., and Garnier, J. 2012. Evaluation of the efficiencies of helical anchor plates in sand by centrifuge model tests. Canadian Geotechnical Journal, **49**(9): 1102–1114. doi:Doi 10.1139/T2012-064.

Tucker, K.. 1987. Uplift capacity of drilled shafts and driven piles in granular materials. *In* Foundations for transmission line towers. pp. 142–159.

Vermeer, P.A., and Sutjiadi, W. 1985. The uplift resistance of shallow embedded anchors. *In* Proc., of 11th Int. Conf. of Soil Mechanics and Foundation Engineering. Balkema, Rotterdam, The Netherlands, San Francisco, USA. pp. 1635–1638.

Wang, L., Coombs, W.M., Augarde, C.E., Brown, M., Knappett, J., Brennan, A., Richards, D., and Blake, A. 2017. Modelling Screwpile Installation Using the MPM. Procedia Engineering, **175**: 124–132. Elsevier B.V. doi:10.1016/j.proeng.2017.01.040.

White, D.J., Cheuk, C.Y., and Bolton, M.D. 2008. The uplift resistance of pipes and plate anchors buried in sand. Géotechnique, **58**(10): 771–779. doi:10.1680/geot.2008.3692.

Zienkiewicz, O.C., and Taylor, R.L. 2000. The finite element method (vol. 2): Solid mechanics. *In* Vasa, Fifth Edit. Butterworth-Heineman, Oxford, UK.

## FIGURE CAPTION LIST

Figure 1 Comparison of centrifuge tests with respect to relatively large scale 1g, centrifuge and field experimental results, for plate anchors (wished in place, open markers) and screw anchors (installation effect, closed markers). Centrifuge and field tests are underlined by solid and dashed lines respectively. Single and double refer to the number of helices. The Giampa et al. (2017) criterion is calculated for very dense (VD) and medium-dense (MD) soil properties.

Figure 2 Schematic description of the multi-stage methodology

Figure 3 Comparison of the load-displacement relationship for the wished in place centrifuge tests ($H/D_h$ = 6) in dense sand from (Hao et al. 2018) and numerical simulations (Stage 1 & Stage 2 – capacity)

Figure 4 Comparison of wished in place centrifuge tests in dense sand from (Hao et al. 2018) and numerical simulations (Stage 2 – capacity). The two sets of parameters used to calculate the analytical criterion of Giampa et al. (2017) correspond to the maximum and minimum density values.

Figure 5 Comparison of centrifuge test results and finite element simulations (stages 1 & 2). (a) U1VD-A, $H/D_h$ = 5.9; (b) U1MD, $H/D_h$ = 4.5; (c) U1VD-B, $H/D_h$ =7.4; (d) U2VD, $H/D_{h,1}$ =7.4 & $H/D_{h,2}$ = 5.4

Figure 6 Failure mechanism development at different anchor imposed displacements ($u_{y,imposed}$), single helix in very dense sand (U1VD-B, $H/D_h$ = 7.4), the dashed line indicates the failure mechanism assumed by (Giampa et al. 2017).

Figure 7 Failure mechanism development at different anchor imposed displacements ($u_{y,imposed}$), double helix in very dense sand (U2VD, $H/D_h$=7.4& 5.4), the inclined dashed line indicates the failure mechanism assumed by (Giampa et al. 2017).

Figure 8 Comparison of the indicators of failure at the anchor's head ($u_{y,imposed}$), (U1VD-B) and soil-soil interface, the dashed line indicates the soil-soil interface

Figure 9 Consideration of cross-section along the assumed failure mechanism for the single helix embedded in very dense sand (U1VD-B), ξ is the distance from the edge of the plate in the direction of the cross-section, $\tau_{max}$ is the maximum shear stress that could be mobilised (=$\sigma'_N \tan \phi'pk$).

Figure 10 Comparison of the stress distribution along a cross-section (inclined at ψ degrees to the vertical) and along the interface elements for the single helix (U1VD-B), after a vertical displacement $u_y = 0.3D_h$

Figure 11 Consideration of the cross-section along the assumed mechanism (ψ = 17°) for a single helix screw anchor ($D_h$ = 1.7m) embedded at different depths in very dense (VD) sand, stage 1 simulations, ξ is the distance from the edge of the plate in the direction of the cross-section, $\tau_{max}$ is the maximum shear stress that could be mobilised (=$\sigma'_N \tan \phi'pk$).

Figure 12 Normalised distance along the failure plane over which the shear strain $\gamma_s$ is larger or equal to 10% with respect to normalised plate depth

Figure 13 Comparison of bearing factors $N_\gamma$ for a single helix screw anchor ($D_h$ = 1.7m) at two different densities and stage 2 (enhanced capacity). (a) $D_r$ = 57%; (b) $D_r$ = 84%.

Figure 14 Comparison of unloading/reloading Young modulus $E_{ur}$ (a-b) and effective average stress p' (c-d) after a step-installation procedure (a, c) or after a single compression load (b, d). The inclined dashed line indicates the soil-soil interface position in stage 2.

Figure 15 Idealisation of the installation effect on the soil behaviour, based on the small-strain Hardening soil model. (a) Effect of previous shearing; (b) Effect of average stress increase.

Figure 16 Comparison of centrifuge (U1VD-A, $H/D_h$ = 5.9) and numerical solutions with different imposed failure mechanisms.

Table caption list

Table 1 Geometry, crowd force (Fy,min) and uplift capacity (Fy) of the different screw pile models at prototype scale for UoD (Davidson et al. 2019) and UWA (Hao et al. 2018) tests

Table 2 Properties of the plate elements (identical for pile core and helices), assumed identical for all tests

Table 3 Number of elements and nodes of the meshes for each simulation (stage 1)

Table 4 HSsmall parameters for the HST95 Congleton sand, (after Al-Defae et al. 2013, Lauder et al. 2013, Al-Baghdadi et al. 2017a), reference stiffness is for a reference pressure $p^{ref}$ = 100kPa.

Table 4 Comparison of the uplift capacity and CPU run time as a function of the mesh refinement for the U1VD-B. The CPU time is normalised with respect to the fastest simulation (mesh #1)

Table 6 Effect of the preloading level ($F_{y0,max}$) on the uplift capacity ($F_y$) of the single deep helix (U1VD-B,)

Table 7 Comparison of the pitch to helix diameter ratio for different studies

# TABLES

Table 1 Geometry, crowd force (Fy,min) and uplift capacity (Fy) of the different screw pile models at prototype scale for UoD (after Davidson et al. 2019) and UWA (after Hao et al. 2018) tests

| | Helix number [-] | $D_r$ [%] | $D_h$ [m] | $D_s$ [m] | H [m] | $H/D_h$ | Pitch [m] | $F_{y,min}$ [MN] | $F_y$ [MN] |
|---|---|---|---|---|---|---|---|---|---|
| UoD tests | | | | | | | | | |
| U1VD-A | 1 | 84 | 1.7 | 0.88 | 10 | 5.9 | 0.56 | -12.5 | 6.4 |
| U1VD-B | 1 | 84 | 1.7 | 0.88 | 12.5 | 7.4 | 0.56 | -18.0 | 10.6 |
| U2VD | 2 | 84 | 1.7 | 0.88 | 9.1/12.5 | 5.4/7.4 | 0.56 | -20.2 | 10.8 |
| U1MD | 1 | 57 | 3.4 | 1.13 | 15.2 | 4.5 | 0.56 | -21.0 | 15 |
| UWA tests | | | | | | | | | |
| SP3 | 1 | 85.8 | 0.4 | 0.094 | 1.2 | 3 | 0.1 | | 0.023 |
| SP6 | 1 | 85.8 | 0.4 | 0.094 | 2.4 | 6 | 0.1 | | 0.109 |
| SP9 | 1 | 85.8 | 0.4 | 0.094 | 3.6 | 9 | 0.1 | | 0.236 |
| SP12-a | 1 | 85.5 | 0.4 | 0.094 | 4.8 | 12 | 0.1 | | 0.358 |
| SP12-b | 1 | 85.4 | 0.4 | 0.094 | 4.8 | 12 | 0.1 | | 0.313 |
| SH2 | 1 | 86.7 | 0.4 | 0.094 | 0.8 | 2 | 0.1 | | 0.001 |
| SH3-a | 1 | 86.4 | 0.4 | 0.094 | 1.2 | 3 | 0.1 | | 0.022 |
| SH3-b | 1 | 96.2 | 0.4 | 0.094 | 1.2 | 3 | 0.1 | | 0.023 |
| SH4 | 1 | 86.7 | 0.4 | 0.094 | 1.6 | 4 | 0.1 | | 0.043 |
| SH6-a | 1 | 86.4 | 0.4 | 0.094 | 2.4 | 6 | 0.1 | | 0.108 |
| SH6-c | 1 | 96.2 | 0.4 | 0.094 | 2.4 | 6 | 0.1 | | 0.122 |
| SH7.5 | 1 | 90.0 | 0.4 | 0.094 | 3.0 | 7.5 | 0.1 | Wished-in-Place | 0.162 |
| SH8-a | 1 | 86.4 | 0.4 | 0.094 | 3.2 | 8 | 0.1 | | 0.176 |
| SH8-b | 1 | 96.4 | 0.4 | 0.094 | 3.2 | 8 | 0.1 | | 0.218 |
| SH9-a | 1 | 88.8 | 0.4 | 0.094 | 3.6 | 9 | 0.1 | | 0.250 |
| SH9-b | 1 | 96.1 | 0.4 | 0.094 | 3.6 | 9 | 0.1 | | 0.270 |
| SH9-c | 1 | 96.2 | 0.4 | 0.094 | 3.6 | 9 | 0.1 | | 0.260 |
| SH10 | 1 | 96.4 | 0.4 | 0.094 | 4.0 | 10 | 0.1 | | 0.310 |
| SH10.5 | 1 | 90.0 | 0.4 | 0.094 | 4.0 | 10.5 | 0.1 | | 0.272 |
| SH12-a | 1 | 85.4 | 0.4 | 0.094 | 4.8 | 12 | 0.1 | | 0.322 |
| SH12-b | | 91.7 | 0.4 | 0.094 | 4.8 | 12 | 0.1 | | 0.365 |

Table 2 Properties of the plate elements (identical for pile core and helices), assumed identical for all tests

| EA [GN/m] | EI [MNm²/m] | $t_{equiv}$ [m] | ν [-] |
|---|---|---|---|
| 38.08 | 39.8 | 0.112 | 0.3 |

Table 3 Number of elements and nodes of the meshes for each simulation (stage 1). The minimum element size was normalised with respect to the helix diameter $D_h$.

| | | Elements | Min El. Size/$D_h$ [-] | Nodes |
|---|---|---|---|---|
| UoD | U1VD-A | 2534 | 0.03 | 21206 |
| | U1VD-B | 3175 | 0.04 | 26476 |
| | U2VD | 3779 | 0.03 | 31428 |
| | U1MD | 3674 | 0.03 | 30296 |
| UWA | SH2 | 3888 | 0.05 | 31770 |
| | SH4 | 3514 | 0.05 | 28918 |
| | SH6 | 4517 | 0.05 | 37128 |
| | SH7.5 | 6382 | 0.05 | 52002 |
| | SH9 | 5187 | 0.05 | 42448 |

Table 4 HSsmall parameters for the HST95 Congleton sand, after (after Lauder et al. 2013; Al-Defae et al. 2013; Al-Baghdadi et al. 2017a), reference stiffness is for a reference pressure $p^{ref}$ = 100kPa.

| Soil parameters | | Unit | Equation | $D_r$ = 57% | $D_r$ = 84% |
|---|---|---|---|---|---|
| Min. void ratio | $e_{min}$ | [-] | | 0.469 | 0.469 |
| Max. void ratio | $e_{max}$ | [-] | | 0.769 | 0.769 |
| Initial void ratio | $e_0$ | [-] | | 0.597 | 0.515 |
| Peak friction angle | $\phi'_{pk}$ | [°] | $20I_D + 29$ | 40.4 | 45.8 |
| Dilatancy angle | $\psi$ | [°] | $25I_D - 4$ | 10.25 | 17 |
| Effective apparent cohesion | c' | [kPa] | $25I_D + 20.22$ | 1.0 | 1.0 |
| Oedometer stiffness | $E_{oed}^{ref}$ | [MPa] | $25I_D + 20.22$ | 34.5 | 41.2 |
| Secant stiffness | $E_{50}^{ref}$ | [MPa] | $1.25E_{oed}^{ref}$ | 43.1 | 51.5 |
| Unloading/reloading stiffness | $E_{ur}^{ref}$ | [MPa] | $3E_{oed}^{ref}$ | 103.4 | 123.7 |
| Material parameter | M | [-] | $0.6 - 0.1\, I_D$ | 0.54 | 0.52 |
| Unloading/reloading Poisson's ratio | $\nu_{ur}$ | [-] | | 0.2 | 0.2 |
| Reference shear strain | $\gamma_{0.7}$ | [-] | $(1.7I_D + 0.67) \cdot 10^{-4}$ | $1.64 \cdot 10^{-4}$ | $2.09 \cdot 10^{-4}$ |
| Low strain shear modulus | $G_0^{ref}$ | [MPa] | $50I_D + 88.8$ | 118.8 | 130.8 |
| Total unit weight | $\gamma_{tot}$ | [kN/m³] | $30I_D + 14.5$ | 19.83 | 20.30 |

Table 5 Comparison of the uplift capacity and CPU run time as a function of the mesh refinement for the U1VD-B (stage 1 simulation). The CPU time is normalised with respect to the fastest simulation (mesh #1). The average, maximum and minimum element sizes were normalised with respect to the helix diameter. The computer used had the following specifications: Intel® Xeon® CPU E5-1650 v4 @3.60GHz, 24GB RAM, 64-bit operating system.

| Mesh | | 1 | 2 | 3 | 4 | 5 |
|---|---|---|---|---|---|---|
| Elements | [-] | 498 | 808 | 2175 | 3175 | 5678 |
| Average El. size/$D_h$ | [-] | 0.94 | 0.73 | 0.37 | 0.29 | 0.22 |
| Max El. Size/$D_h$ | [-] | 3.75 | 2.75 | 2.08 | 2.61 | 1.91 |
| Min El. Size/$D_h$ | [-] | 0.15 | 0.11 | 0.04 | 0.04 | 0.03 |
| Nodes | [-] | 4337 | 6878 | 18292 | 26746 | 46866 |
| $F_{y,0.1D_h}$ | [MN] | 13.78 | 12.95 | 13.64 | 13.35 | 13.13 |
| $F_{y,max}$ | [MN] | 14 | 14.83 | 14.58 | 15.09 | 15.23 |
| Normalised CPU time | [s] | 1 | 3.4 | 19.2 | 24.4 | 46.7 |

Table 6 Effect of the preloading level ($F_{y0,max}$) on the uplift capacity ($F_y$) of the single deep helix (U1VD-B)

| $F_{y0,max}$ [MN] | $F_y$ [MN] |
|---|---|
| -9 | 10.9 |
| -18 | 11.3 |
| -27 | 12.1 |

# FIGURES

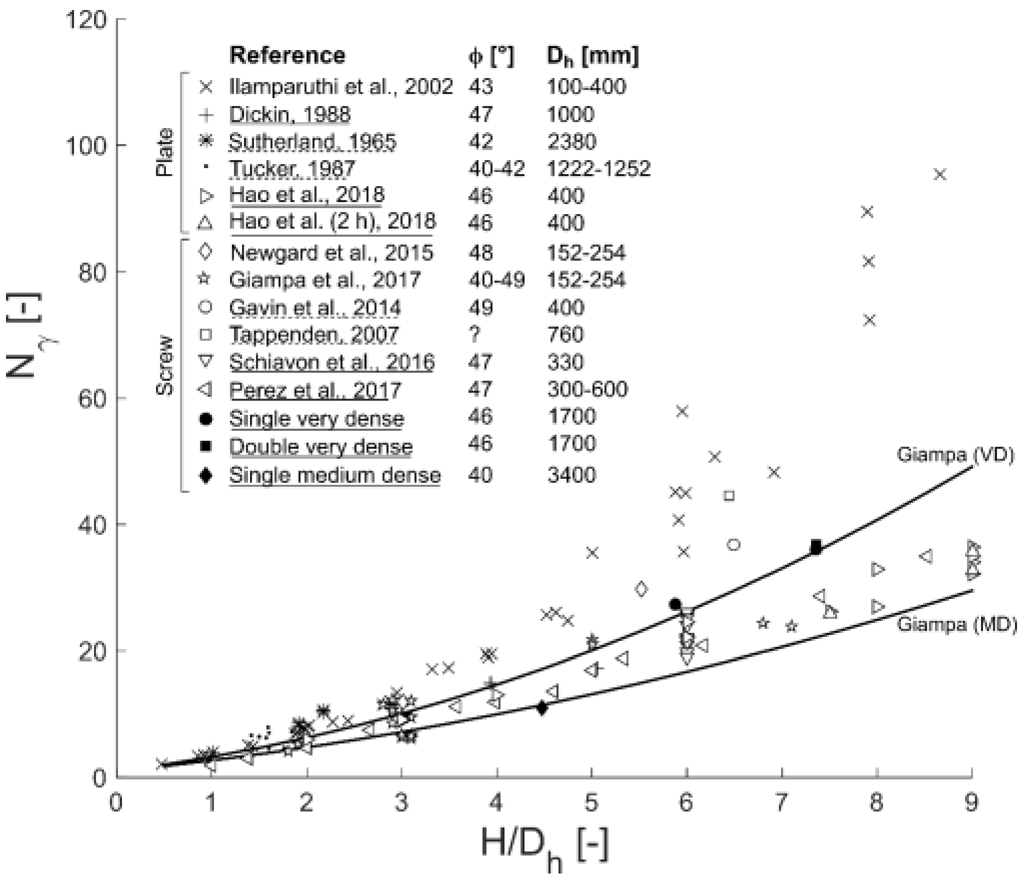


Figure 1 Comparison of centrifuge tests with respect to relatively large scale 1g, centrifuge and field experimental results, for plate anchors (wished in place, open markers) and screw anchors (installation effect, closed markers).

Centrifuge and field tests are underlined by solid and dashed lines respectively. Single and double refer to the number of helices. The Giampa et al. (2017) criterion is calculated for very dense (VD) and medium-dense (MD) soil properties.

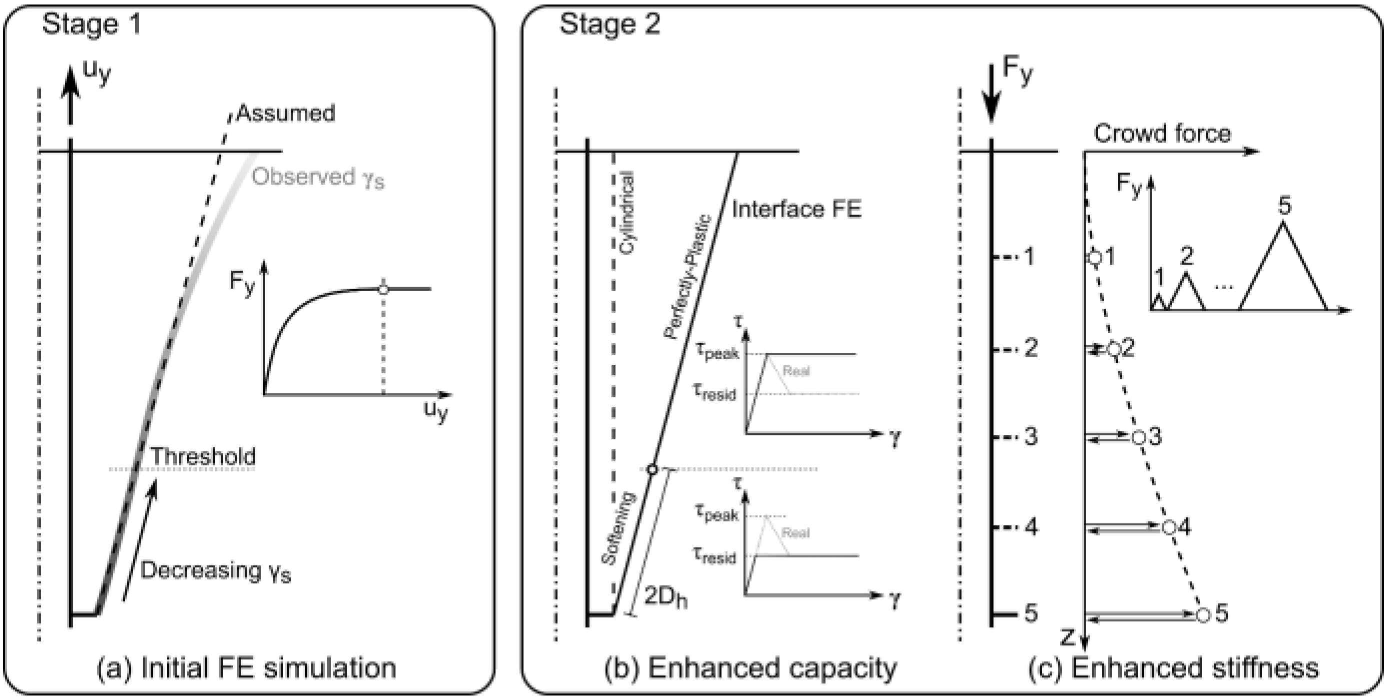


Figure 2 Schematic description of the multi-stage methodology

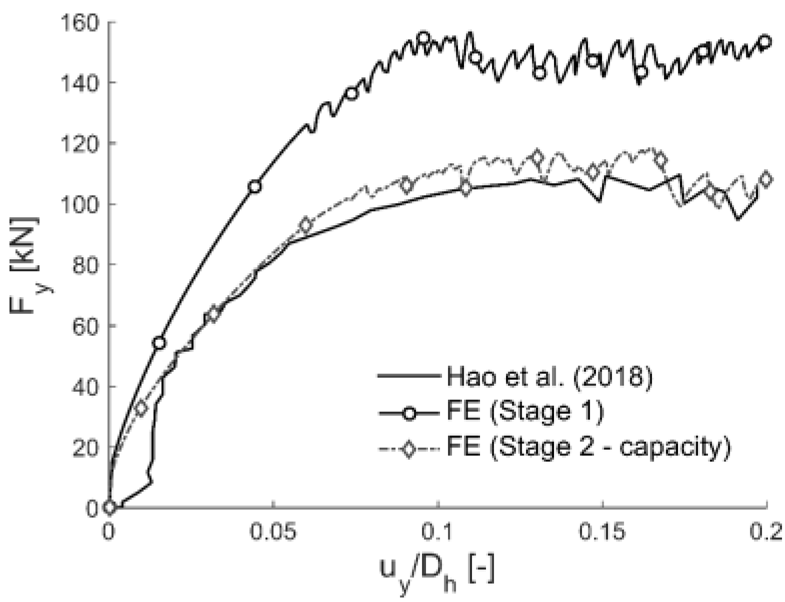


Figure 3 Comparison of the load-displacement relationship for the wished in place centrifuge tests ($H/D_h$ = 6) in dense sand from Hao et al. (2018) and numerical simulations (Stage 1 & Stage 2 – capacity)

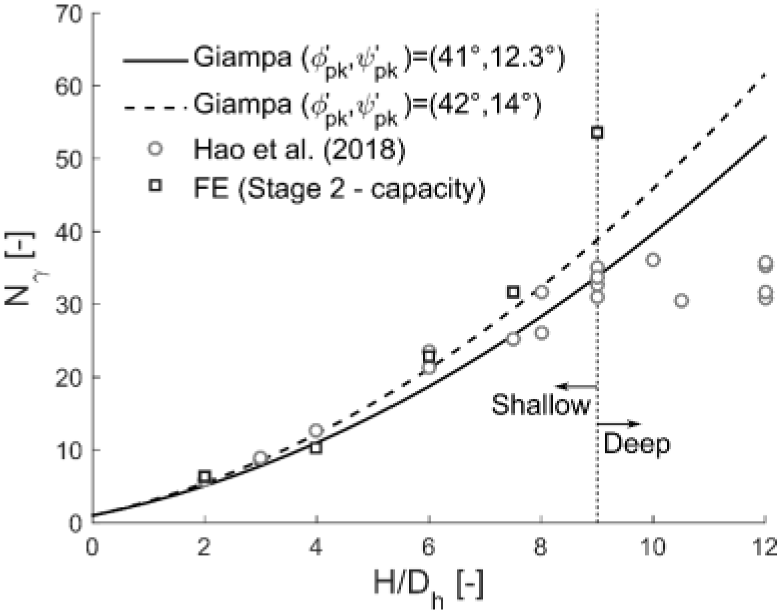


Figure 4 Comparison of wished in place centrifuge tests in dense sand from Hao et al. (2018) and numerical simulations (Stage 2 – capacity). The two sets of parameters used to calculate the analytical criterion of Giampa et al. (2017) correspond to the maximum and minimum density values.

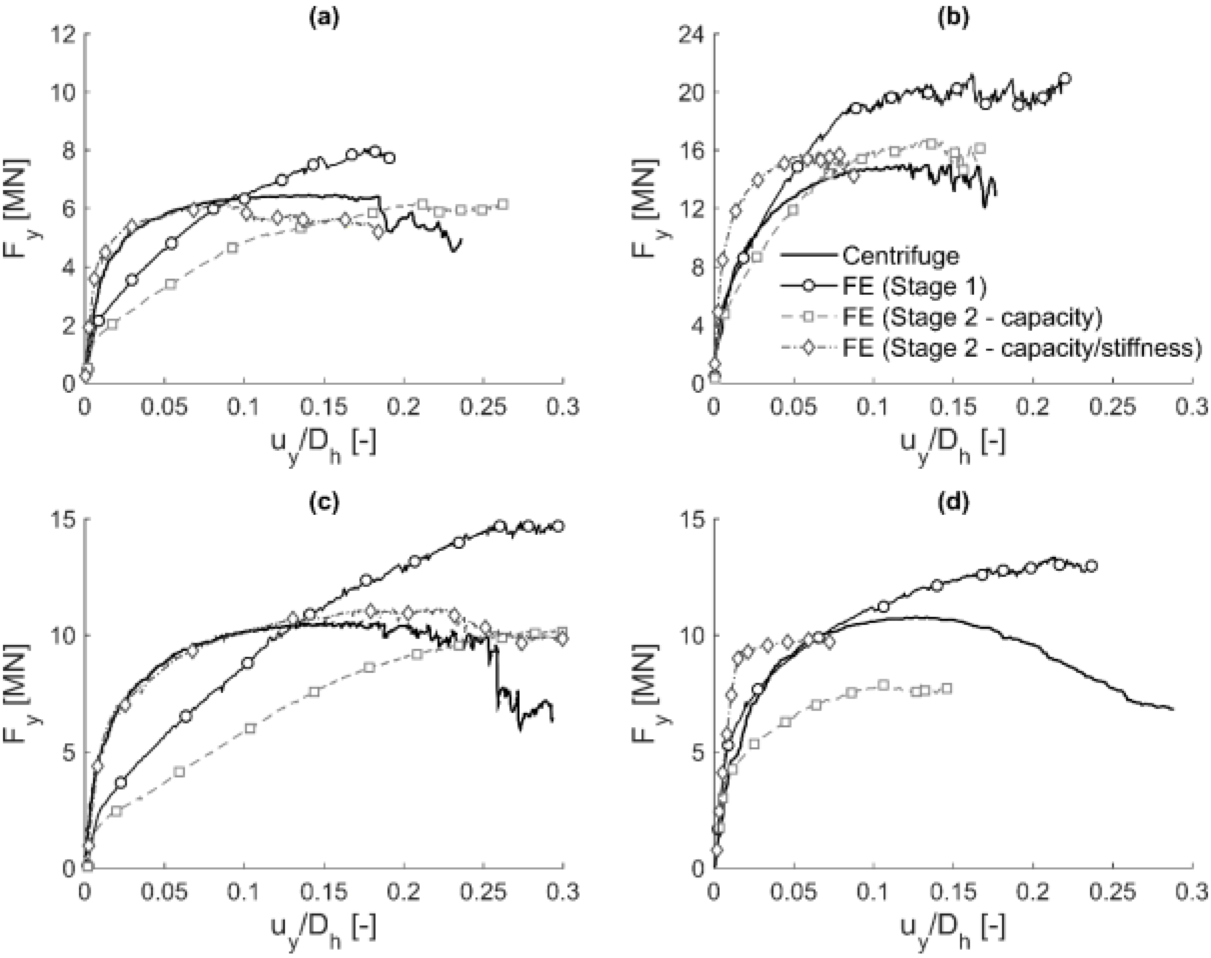


Figure 5 Comparison of centrifuge test results and finite element simulations (stages 1 & 2). (a) U1VD-A, $H/D_h$ = 5.9; (b) U1MD, $H/D_h$ = 4.5; (c) U1VD-B, $H/D_h$ =7.4; (d) U2VD, $H/D_{h,1}$ =7.4 & $H/D_{h,2}$ = 5.4

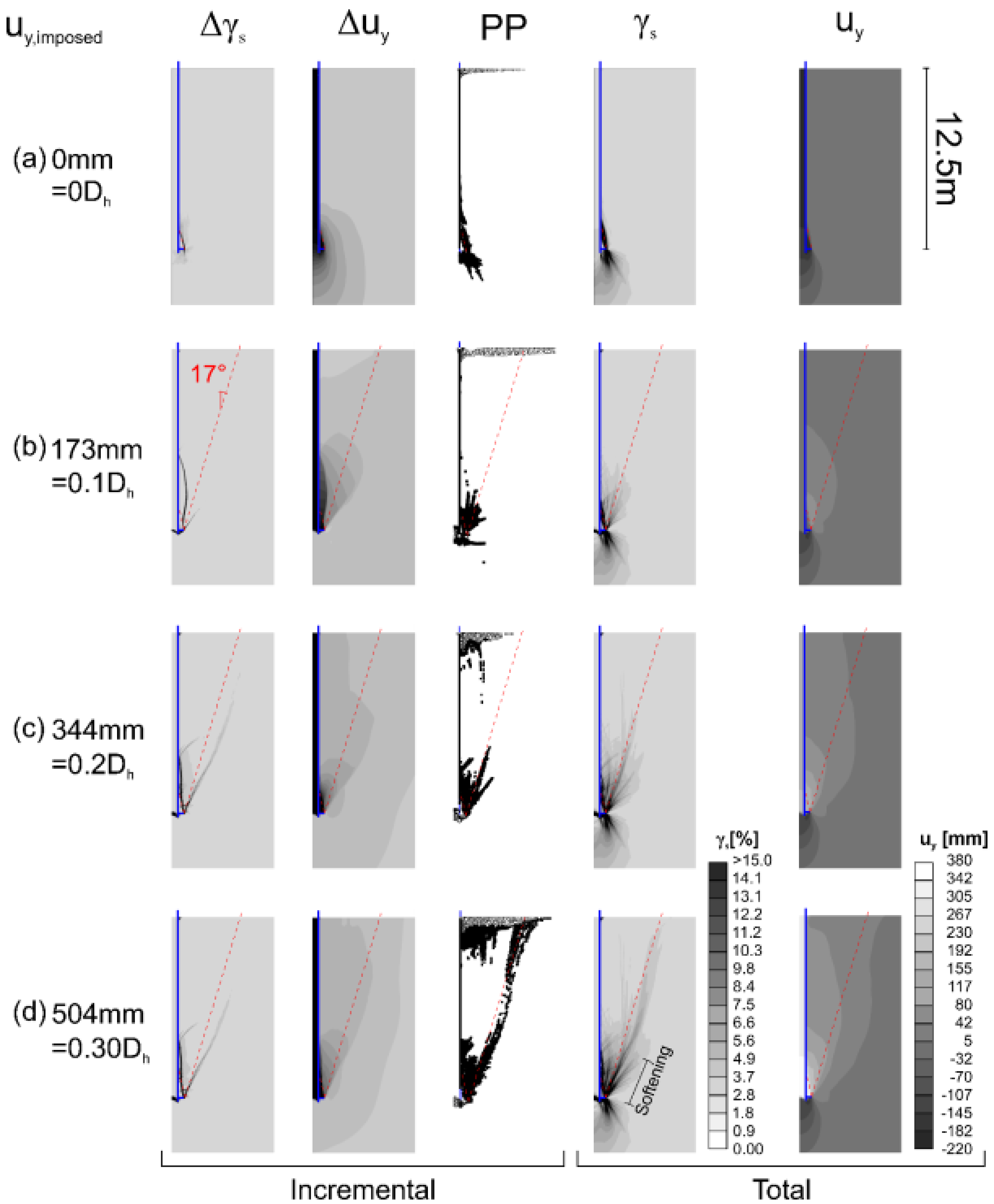


Figure 6 Failure mechanism development at different anchor imposed displacements ($u_{y,imposed}$), single helix in very dense sand (U1VD-B, $H/D_h$ = 7.4), the dashed line indicates the failure mechanism assumed by Giampa et al. (2017).

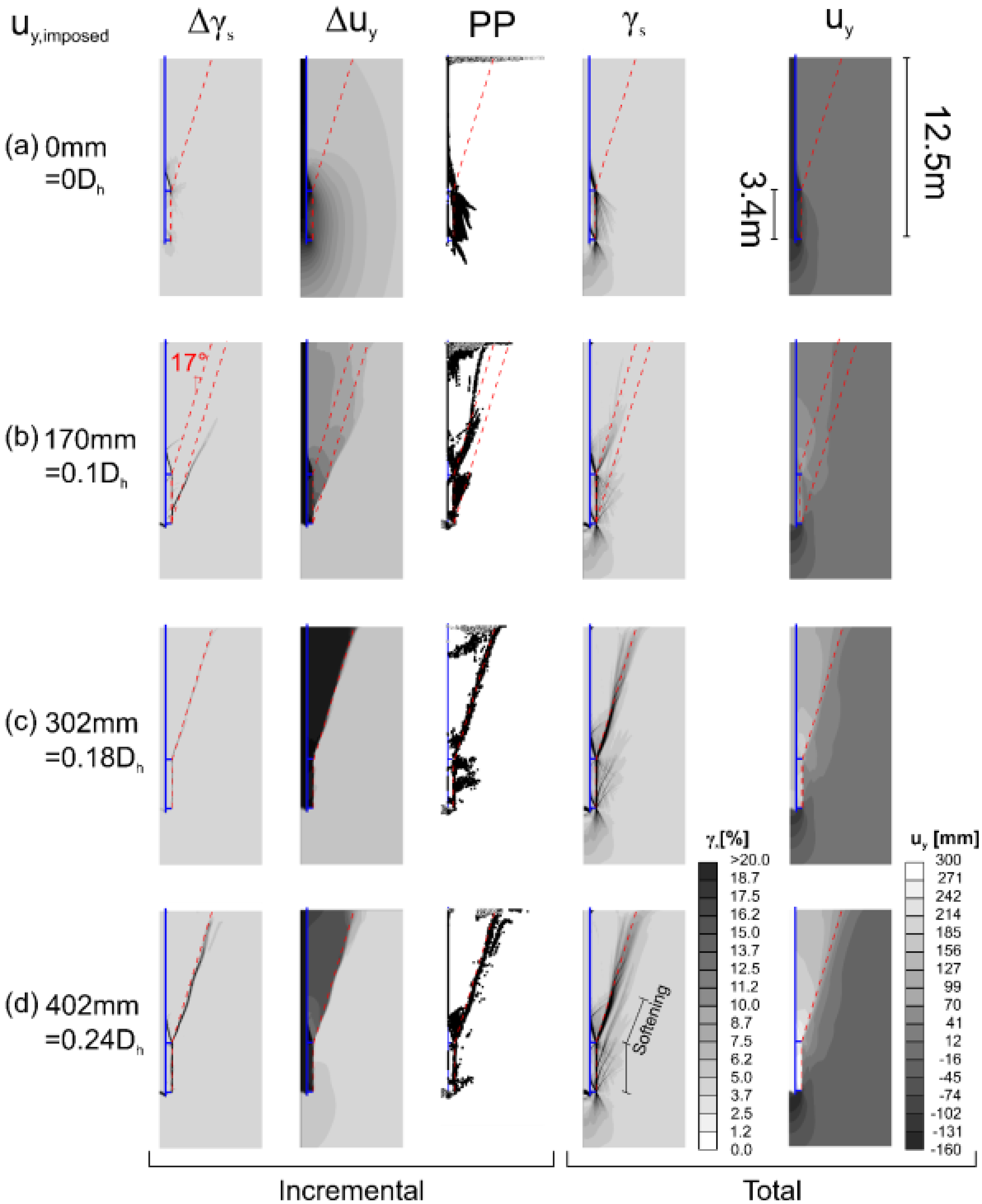


Figure 7 Failure mechanism development at different anchor imposed displacements ($u_{y,imposed}$), double helix in very dense sand (U2VD, $H/D_h$=7.4& 5.4), the inclined dashed line indicates the failure mechanism assumed by Giampa et al. (2017).

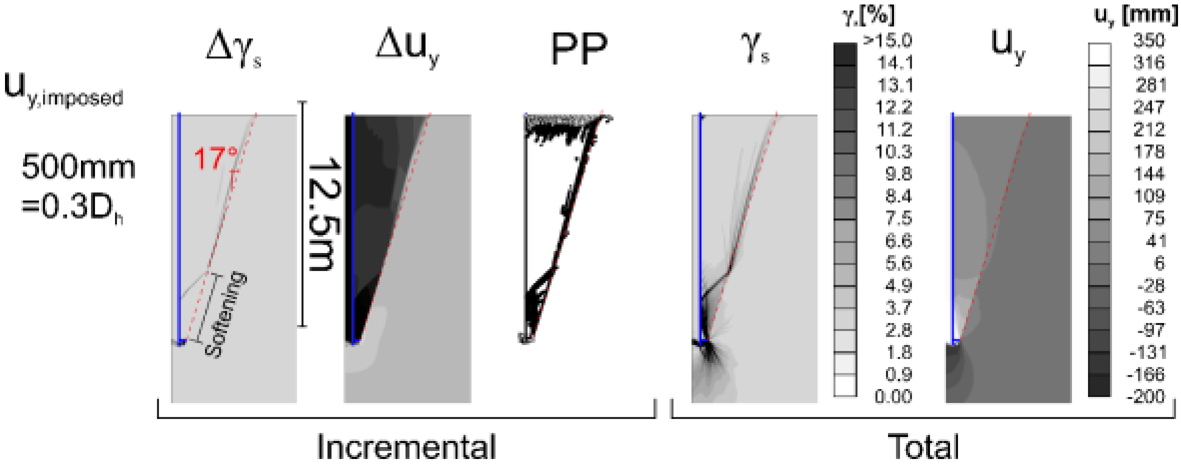


Figure 8 Comparison of the indicators of failure at the anchor's head ($u_{y,imposed}$), (U1VD-B) and soil-soil interface, the dashed line indicates the soil-soil interface

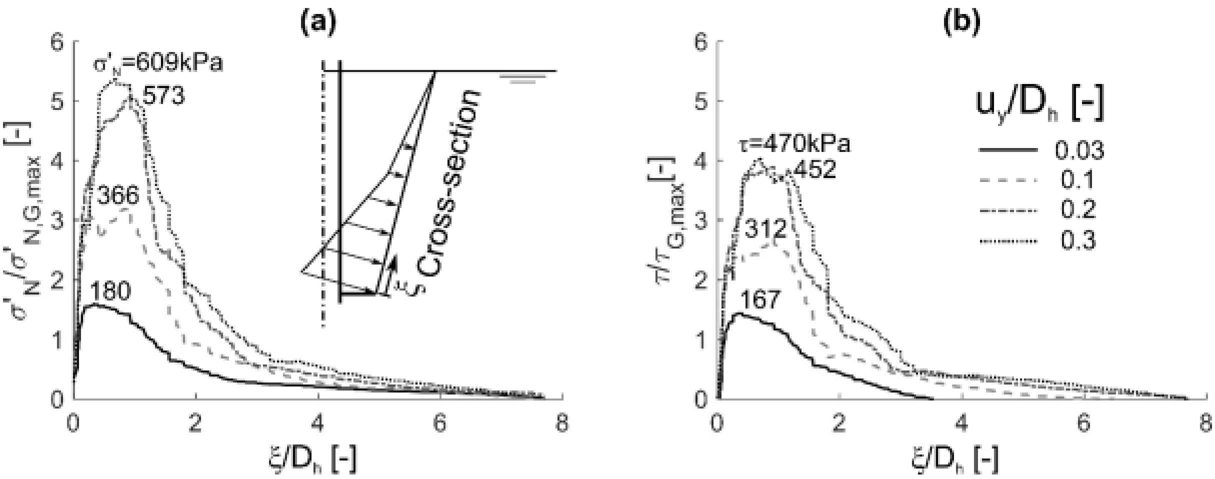


Figure 9 Consideration of cross-section along the assumed failure mechanism for the single helix embedded in very dense sand (U1VD-B), ξ is the distance from the edge of the plate in the direction of the cross-section, $\tau_{max}$ is the maximum shear stress that could be mobilised (=$\sigma'_N$ tan $\phi'_{pk}$).

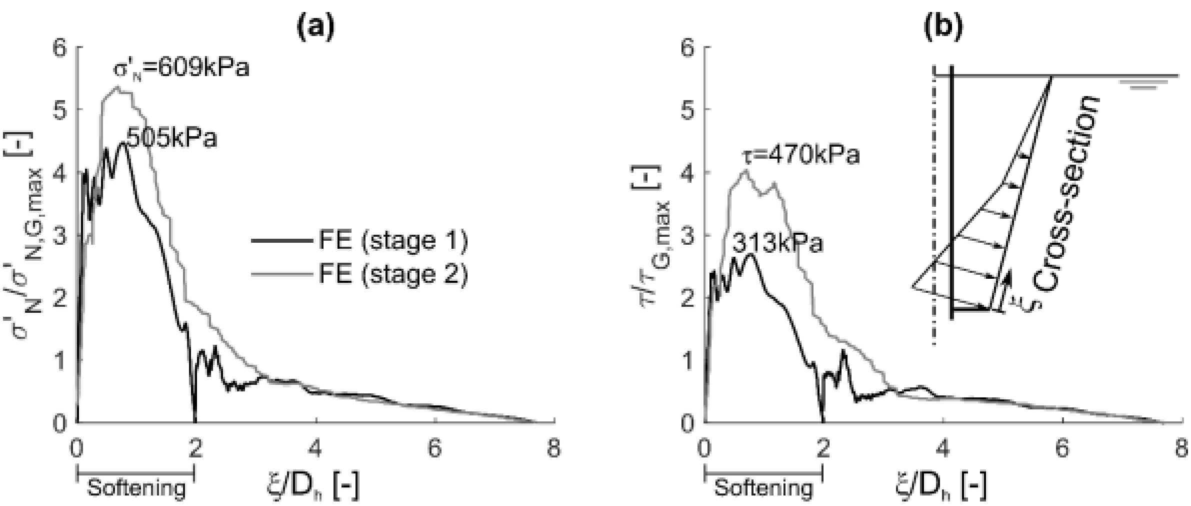


Figure 10 Comparison of the stress distribution along a cross-section (inclined at ψ degrees to the vertical) and along the interface elements for the single helix (U1VD-B), after a vertical displacement $u_y$ = 0.3D$_h$

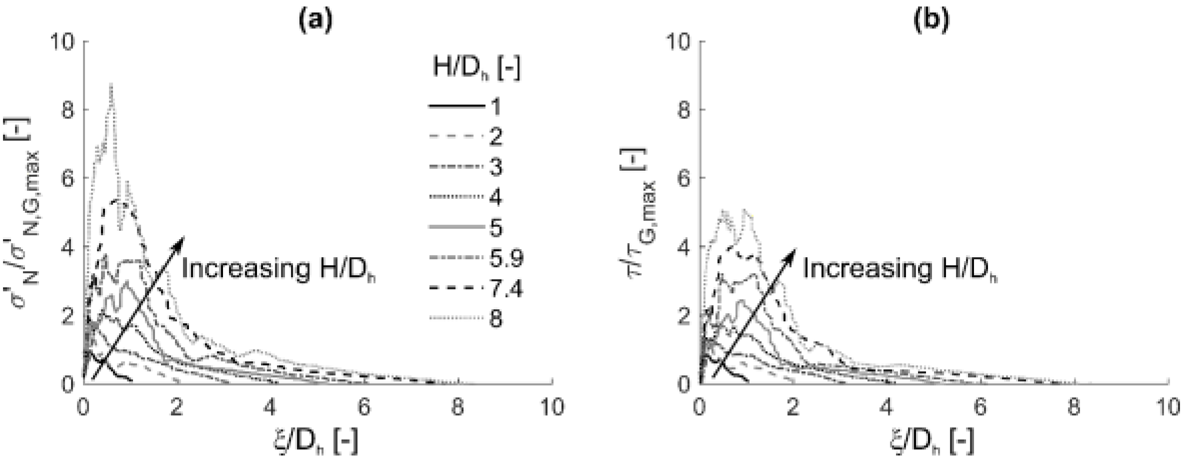


Figure 11 Consideration of the cross-section along the assumed mechanism ($\psi$ = 17°) for a single helix screw anchor ($D_h$ = 1.7m) embedded at different depths in very dense (VD) sand, stage 1 simulations, $\xi$ is the distance from the edge of the plate in the direction of the cross-section, $\tau_{max}$ is the maximum shear stress that could be mobilised (=$\sigma'_N$ tan $\phi'_{pk}$).

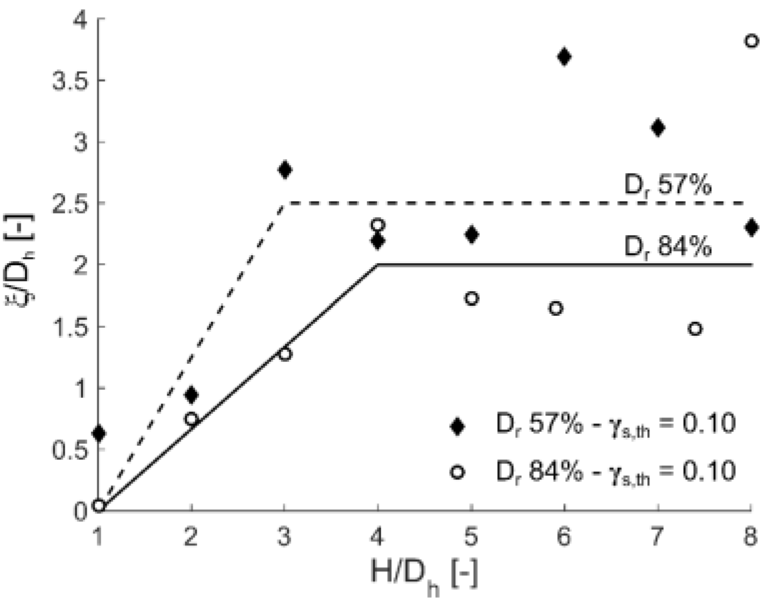


Figure 12 Normalised distance along the failure plane over which the shear strain $\gamma_s$ is larger or equal to 10% with respect to normalised plate depth

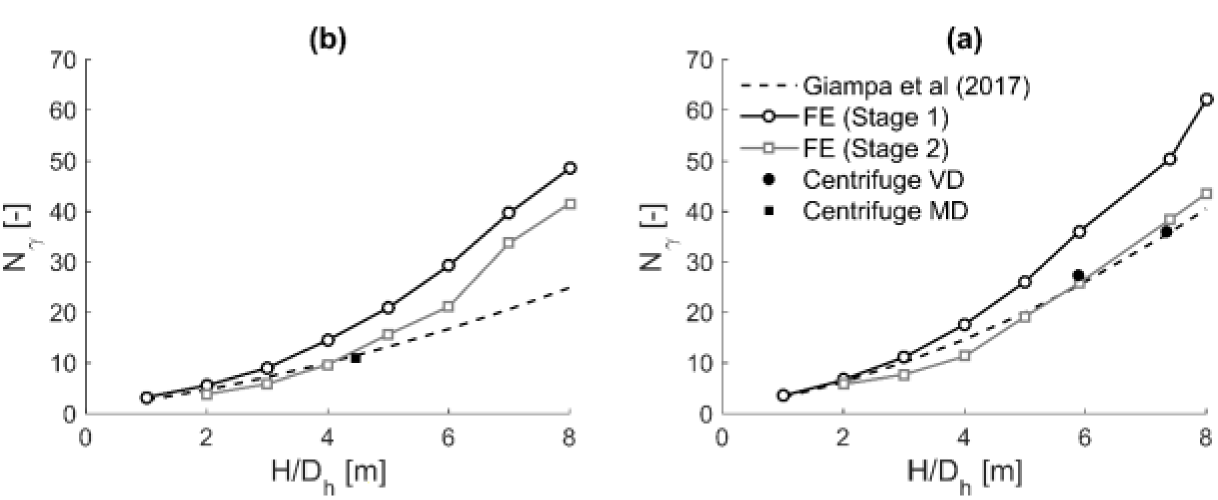


Figure 13 Comparison of bearing factors $N_\gamma$ for a single helix screw anchor ($D_h$ = 1.7m) at two different densities and stage 2 (enhanced capacity). (a) $D_r$ = 57%; (b) $D_r$ = 84%.

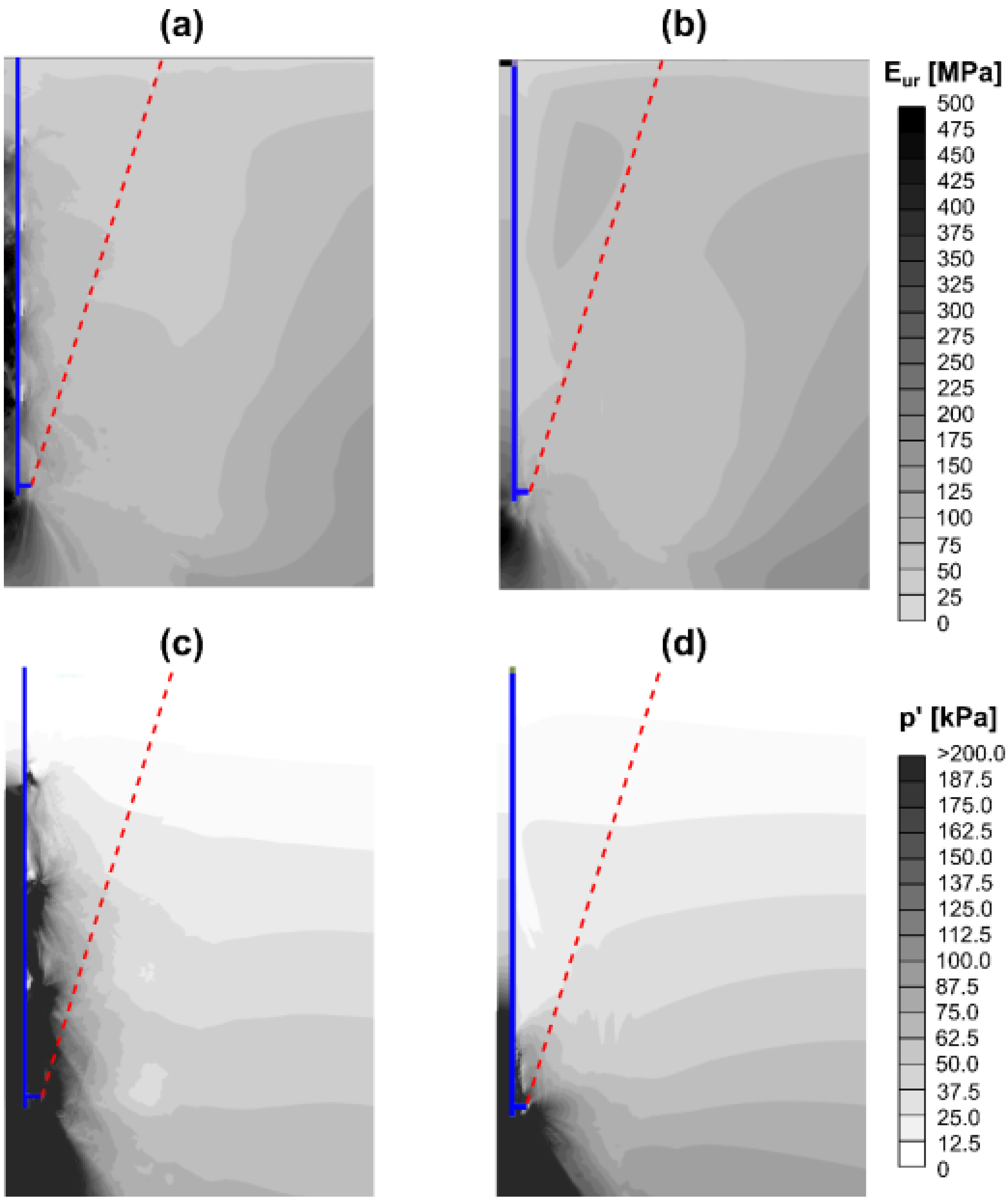


Figure 14 Comparison of unloading/reloading Young modulus $E_{ur}$ (a-b) and effective average stress p' (c-d) after a step-installation procedure (a, c) or after a single compression load (b, d). The inclined dashed line indicates the soil-soil interface position in stage 2.

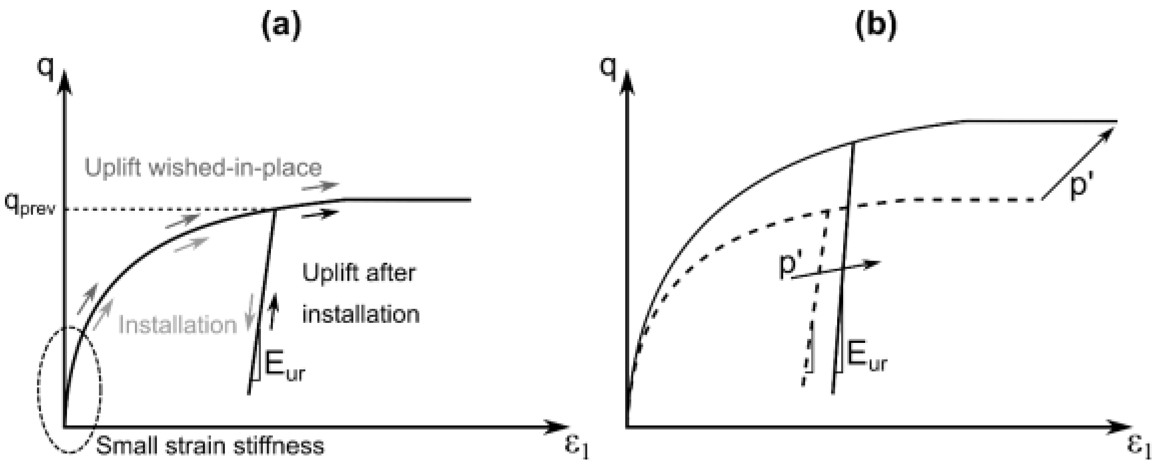

Figure 15 Idealisation of the installation effect on the soil behaviour, based on the small-strain Hardening soil model. (a) Effect of previous shearing; (b) Effect of average stress increase.

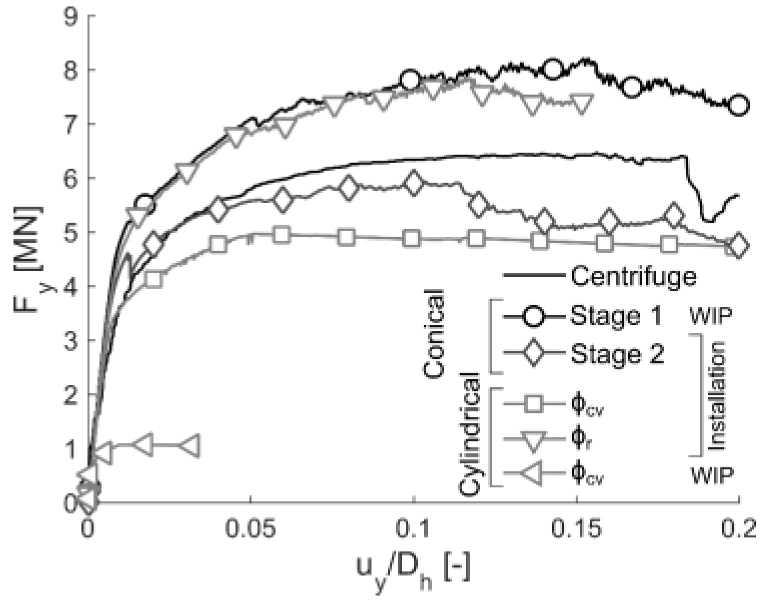


Figure 16 Comparison of centrifuge (U1VD-A, $H/D_h$ = 5.9) and numerical solutions with different imposed failure mechanisms. Simulations include the installation process (Installation) or are wished-in-place (WIP)